



































































































min. After the 20 minutes incubation the cells were analysed using the Muse flow cytometer (Luminex Corporation, Austin, TX 78727, U.S.A.) using the Annexin V & Dead Cell analysis tool. Before the assay can be run, the gating and markers needs to be checked to make sure it is correct. The Muse makes use of forward scatter only, and it can only detect red and yellow fluorescence. Therefore, even though each Muse kit is completely optimised, the user is required to make sure that the gated population is correct (cells and not debris), this was done using the VC to optimize data acquisition. The Muse gives stepwise assistance in the experimental optimisation. The Muse acquires 2000 events per sample, this is based on the optimizations for each assay. The apoptosis profile is divided into 4 quadrants. Quadrant 1 contains non-apoptotic/ live cells that are Annexin V and 7-AAD negative. The second quadrant contains the early apoptotic cells that are Annexin V positive but 7-AAD negative. Quadrant 3 contains the late stage apoptotic to dead cells, they are both Annexin V and 7-AAD positive. The fourth quadrant contain mostly nuclear debris that is Annexin V negative but 7-AAD positive. The results were analysed using Excel and GraphPad Prism 8.1, gating and apoptosis profile graphs were acquired from the Muse software.

## 2.9. Statistical analysis

For the determination of the  $IC_{50}$  of the compound at least three biological and three technical repeats for each biological repeat were performed with different concentration ranges of the compounds and relevant dimethyl sulfoxide (DMSO) vehicle controls. The coefficient of determination ( $R^2$ ), should be  $R^2 \geq 0.90$  for a linear regression model at 95% confidence interval and  $\Delta R \geq 0.1$ . For mechanistic studies treatment groups (vehicle control (VC) and compound(s)) were compared using unpaired, parametric Welch's-tests. The vehicle control was normalized to 100 % and the comparisons were made relative to the VC and presented in percentage form. All statistics were calculated using GraphPad Prism. Experiments performed individually are presented as standard deviations from the mean. Means are presented in bar charts and T-bars are used to indicate standard deviations. p-values less than 0.05 ( $p \leq 0.05$ ) are considered statistically significant.

### 3. Results

The results of both the *in silico* screening and *in vitro* analysis follows here.

#### 3.1. *In silico* screening results

The validation of the crystal structures for use in docking, using an enrichment protocol with known ligands and decoys, yielded results tabulated in table 3.1. Most of the crystal structures had proven sufficiently effective at discriminating between decoys and ligands, save for two AURKA crystal structures, namely 4ZS0 and 4ZTR. They had AUC values below 7 and were thus excluded from further experimentation. The ROC curves in Figure 3.1 of the BRD4 enrichment is an illustration of the effect of ensemble enrichment versus docking into a single crystal structure. By docking into more than one crystal structure, each with slight differences in the binding pocket due to varied inhibitors complexed with it, enables the docking software to mimic induced fit models of protein-ligand binding<sup>104</sup>. It greatly increases the chances of identifying a potential hit, and at the same time it can greatly decrease the odds of identifying false positive hits<sup>104</sup>. The intent was to select a diverse set of crystal structure for each protein based on different inhibitors complexed in the crystal structure as well as the resolution of the crystal structure. Based on the enrichment metrics this paid off.

Table 3. 1: Table of protein crystal structures with enrichment values (AUC).

PDB ID	AUC	7<AUC≤1	PDB ID	AUC	7<AUC≤1
<b>BRD4</b>			<b>AURKB</b>		
3MXF	0.842	Yes	4C2V	0.806	Yes
4BJX	0.783	Yes	5EYK	0.763	Yes
4CL9	0.816	Yes	5K3Y	0.774	Yes
4F3I	0.787	Yes	<b>PLK1</b>		
4OGI	0.838	Yes	3P34	0.787	Yes
5ACY	0.825	Yes	3P36	0.852	Yes
5F60	0.822	Yes	3Q1I	0.783	Yes
5F61	0.805	Yes	4DFW	0.770	Yes
5F63	0.814	Yes	4LKL	0.813	Yes
<b>AURKA</b>			4RCP	0.786	Yes

PDB ID	AUC	7<AUC≤1	PDB ID	AUC	7<AUC≤1
2BMC	0.812	Yes	<b>EGFR</b>		
2J50	0.800	Yes	3UG2	0.745	Yes
3D15	0.715	Yes	4G5J	0.744	Yes
3E5A	0.736	Yes	4G5P	0.802	Yes
3FDN	0.729	Yes	4HJO	0.826	Yes
3P9J	0.814	Yes	4I22	0.776	Yes
4JBQ	0.760	Yes	4WKQ	0.802	Yes
4ZS0	0.679	No	4ZAU	0.807	Yes
4ZTR	0.677	No	5X2K	0.757	Yes
4ZTS	0.792	Yes	5XDK	0.768	Yes
5EW9	0.840	Yes	5XDL	0.764	Yes
<b>AURKB</b>			5ZWJ	0.807	Yes
2BFY	0.740	Yes			
4AF3	0.793	Yes			
4B8M	0.803	Yes			

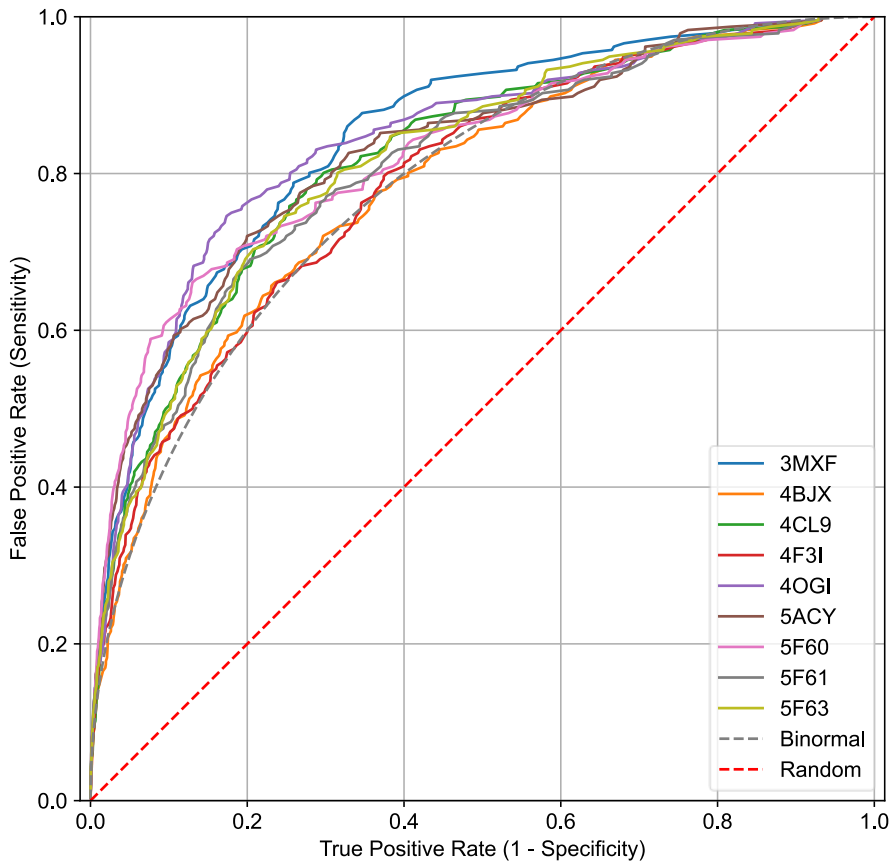
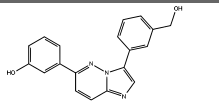
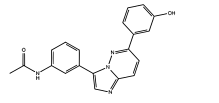
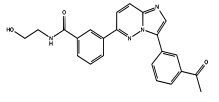
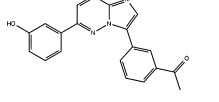
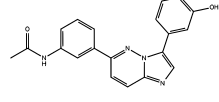
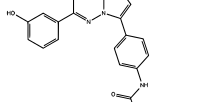
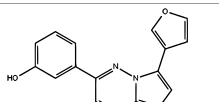
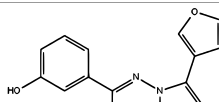
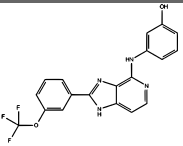
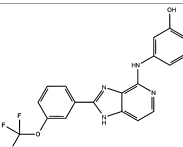


Figure 3. 1: A ranked overlay of all the ROC-curves generated for all the BRD4 protein crystal structures. The binormal curve serves as the predictive function of enrichment. Enrichment serves to normalize the ability of the model to discriminate between false and true positives.

Table 3. 2: Table of the lead compounds, with the compound names, their 2D structure and docking score in each target protein.

Compound	2D Structure	Docking Score			
		BRD4	AURKA	AURKB	EGFR
D2		-9.010	-9.964	-9.585	-10.631
D3		-9.305	-9.773	-9.320	-10.518
D4		-9.005	-10.406	-9.216	-10.256
D5		-9.125	-9.078	-9.354	-10.074
D6		-9.116	-9.590	-9.043	-9.821
D7		-9.357	-9.022	-10.511	-9.630
D8		-9.036	-9.134	-9.374	No binding
D9		-9.252	-9.294	No binding	No binding

Compound	2D Structure	Docking Score			
		BRD4	AURKA	AURKB	EGFR
D10		-9.511	-9.053	No binding	No binding
D11		-9.121	-9.041	No binding	No binding

The docking of the prepared Biofocus library (48 000 structures of which only 20 000 is unique, the rest are stereoisomers, tautomers and different protonation states of these unique ligands) of compounds into the ensemble of BRD4 crystal structures yielded 79 hits (with a docking score  $\leq -9$ , in other words the binding free energy is low, an indication of high binding affinity). Of these 79 compounds only 26 compounds were unique. Thus from 20 000 compounds, 26 potential hits were identified, meaning the BRD4 screening had a hit rate of 0.13%. Most of the compounds had imidazo[1,2-*b*]pyridazine, 1*H*-imidazo[4,5-*c*]pyridine, or 1*H*-indazole backbones. These 79 ligands were then docked into the different kinases, the results of which can be viewed in table 3.2. The naming of the compounds was arbitrarily based upon their location in the 96 well plate they were supplied in. Only ten compounds of the 26 unique ligands were identified as a 'hit' in one or more of the kinases (with a docking score  $\leq -9$ ). There were zero hits for PLK1, thus from here on there will be no referencing with regards to it. Ten compounds successfully docked into the AURKA crystal structures. Seven compounds successfully docked into the AURKB crystal structures (D2-D8). Six compounds successfully docked into the EGFR crystal structures (D2-D7). Compounds D2-D9 have imidazo[1,2-*b*]pyridazine backbones, whereas compounds D10-D11 have 1*H*-imidazo[4,5-*c*]pyridine backbones.

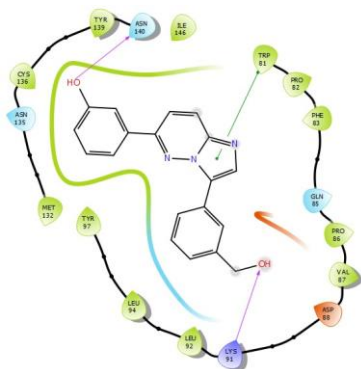
### 3.1.1. BRD4 protein-ligand interactions D2-D11

Hydrogen bond interactions are non-covalent electrostatic interactions between a proton of an electronegative atom (the hydrogen bond donor) and the lone pair of electrons on an electronegative atom (the hydrogen bond acceptor)<sup>105</sup>. The strength of hydrogen bond interactions can vary greatly based upon the distance between the interacting atoms from 8.4 kJ/ mol to 84 kJ/ mol change in free energy ( $-\Delta G$ )<sup>106</sup>. Another non-covalent interaction is known as  $\pi$  interactions. In the instance of  $\pi$ - $\pi$  stacking interactions two aromatic rings, with  $\pi$  bonds, interact with each other<sup>107</sup>. These stacking interactions can be grouped into edge-to-face (T-shaped) interactions, face-to-face stacked interactions, and offset stacked interactions<sup>107</sup>. The strength of  $\pi$ - $\pi$  stacking interactions usually range between 1 kJ/ mol to 50 kJ/ mol<sup>107</sup>. Another  $\pi$  interaction is the  $\pi$ -cation interaction, which are generally stronger than stacking interactions<sup>108</sup>. The  $\pi$ -cation interaction is an electrostatic interaction whereby the electron cloud of a  $\pi$  system interacts with a positively charged cation<sup>108</sup>. These interactions can be quite strong with some studies reporting binding energies of up to 117.2 kJ/mol<sup>108</sup>.

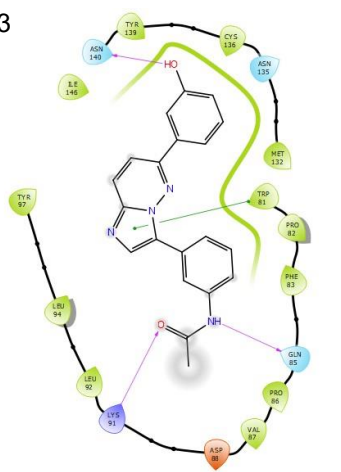
From the ligand-protein interaction diagrams of D2-D11 and BRD4 (Figure 3.2-3.4), a conserved hydrogen bond interaction between asparagine 140 (Asn-140) and hydrogen donors (as well as hydrogen acceptors) of D2-D11 can be observed. Asn-140 is part of the BC loop of the BD1 of BRD4, and plays a very important role in the recognition and hydrogen binding of the acetylated lysine tails of histones<sup>109</sup>. Consequently Asn-140 also play a key role in the binding and stabilization of inhibitors in the binding pocket<sup>81,109</sup>. Tryptophan-81 (Trp-81), which forms part of the ZA loop, also play an important role in the recognition and stabilization of acetylated histone tails inside the binding pocket<sup>109</sup>. In addition to that it has been shown that it also plays a role in the stabilization of inhibitors in the binding pocket<sup>81,109</sup>. Compounds D2, D3, D5, and D7 interacts with Trp-81 by  $\pi$ - $\pi$  stacking, the interaction is between the aromatic side-group of Trp-81 (benzene) and the aromatic backbones of D2, D3, D5, and D7 (imidazole). This interaction is expected to stabilize the inhibitors along the WPF shelf, so named for the conserved Trp-81, proline-82 (Pro-82), and phenylalanine-83 (Phe-83) motif<sup>109-110</sup>. Tyrosine-97 (Tyr-97) of the ZA loop, like Trp81, play an important role in histone as well as stabilization in the binding pocket<sup>109</sup>.

Compounds D6-D9 form bridging hydrogen bonds via a water molecule in the ZA channel with Tyr-97. There is a hydrogen bond interaction between Lysine-91 (Lys-91) and D2, D3, D5, and D6. The positively charged aspartic acid-144 (Asp-144) which forms part of the BC loop, as well as Glycine-85 (Gln-85) seem to play a minor role in acetylated-lysine specificity and inhibitor binding affinities<sup>109</sup>. Compound D4 forms a hydrogen bond with Asp-144, and D9 forms a salt bridge with Asp-144. A hydrogen bond interaction between Gln-85 and D3, D6, D7, D10, and D11<sup>109-111</sup>. Isoleucine-146 (Ile-146), in the  $\alpha$ C helix of BD1 which encloses the hydrophobic WPF shelf, forms a hydrogen bond with D4, this however seems to have minimal overall effects on binding affinities<sup>109</sup>. Pro-82, which forms part of the WPF shelf, has hydrogen bond interactions with compound D10 and D11.

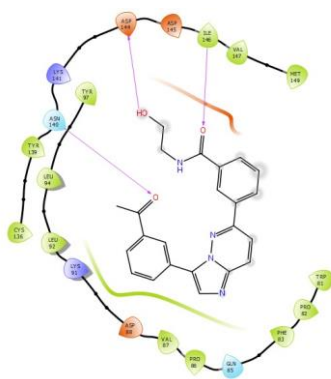
D2



D3



D4



D5

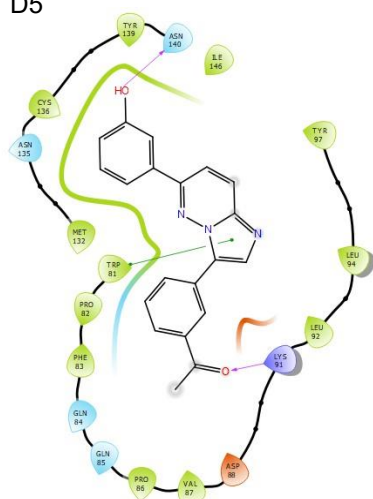
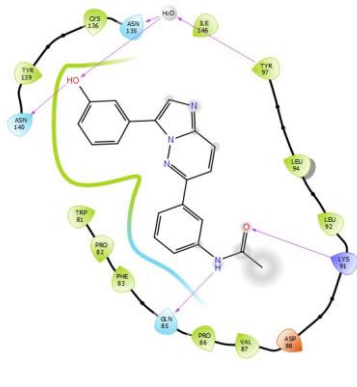
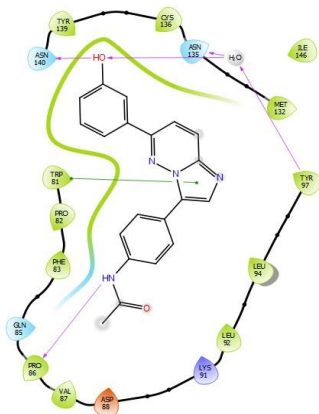


Figure 3. 2: Ligand-protein interaction diagram of D2-D5 complexed with BRD4. Note the hydrogen bond interaction between D2-11 with Asn-140, a conserved interaction that play a key role in effective inhibition. Compounds D2, D3, and D5 interacts with Trp-81 by  $\pi$ - $\pi$  stacking. There is a hydrogen bond interaction between Lys-91 and D2, D3, and D5. D4 forms a hydrogen bond interaction with Asp 144 and Ile-146

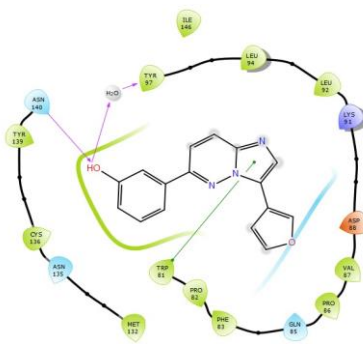
D6



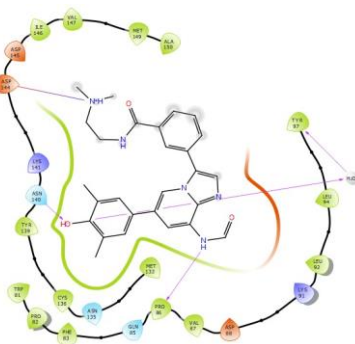
D7



D8



D9



- Charged (negative)
- Charged (positive)
- Glycine
- Hydrophobic
- Metal
- Polar
- Unspecified residue
- Water
- Hydration site
- X Hydration site (displaced)
- Distance
- H-bond
- Halogen bond
- Metal coordination
- Pi-Pi stacking
- Pi-cation
- Salt bridge
- Solvent exposure

Figure 3. 3: Ligand-protein interaction diagram of D6-D9 complexed with BRD4. Note the hydrogen bond interaction between D6-9 with Asn-140, a conserved interaction that play a key role in effective inhibition. Compound D7 interacts with Trp-81 by  $\pi$ - $\pi$  stacking. Compounds D6-D9 form bridging hydrogen bonds via a water molecule in the ZA channel with Tyr-97 and D6 and D7 form an additional interaction with Asn-135. D6 forms a hydrogen bond interaction with Lys-91 and Gln-85. D9 forms a salt-bridge interaction with Asp-144

D10

D11

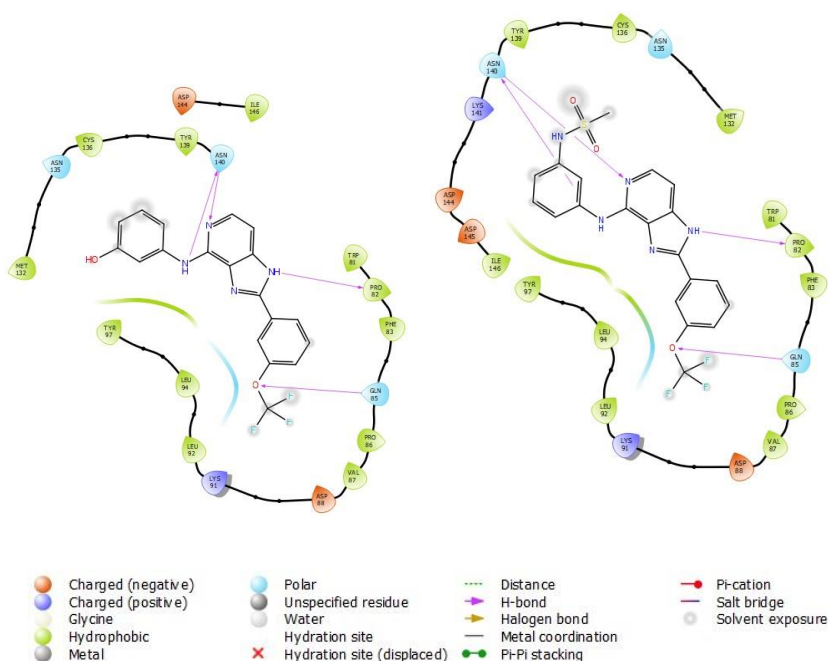


Figure 3. 4: Ligand-protein interaction diagram of D10-D11 complexed with BRD4. Note the hydrogen bond interaction between D10-11 with Asn-140, a conserved interaction that play a key role in effective inhibition. Also notice the hydrogen bond interaction between D10 and 11 with Gln-85 and Pro-82

### 3.1.2.AURKA protein-ligand interactions D2-D11

The ligand interaction diagrams of AURKA and compounds D2-D11 (Figures 3.5-3.7) show promising protein-ligand interactions.

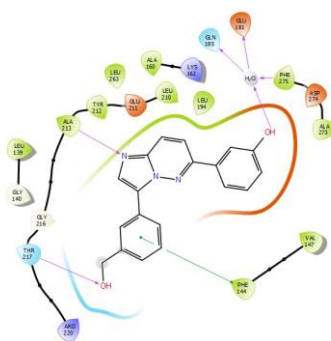
The residues number 210 to 216 in the crystal structure of AURKA, form the hinge region, which plays a significant role in the creation of the AURKA catalytic site within the adenosine triphosphate (ATP) binding pocket<sup>112-113</sup>. The highly conserved alanine-213 (Ala-213) forms part of this hinge region and forms the key interaction between the protein and the ligand<sup>112-113</sup>. Compounds D2, D4, D5, D7, D8, D9, D10, D11, all form hydrogen bond interactions with Ala-213. D2, D4, D7, D8, and D9 act as

hydrogen acceptors, whereas D5 act as a hydrogen donor. D10 and D11 act as both acceptor and donor, forming two hydrogen bonds with Ala-213.

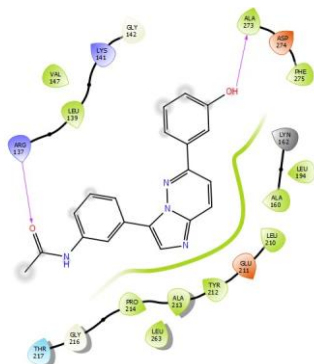
D3 and D5 form hydrogen bond interactions with Ala-273. Threonine-217 (Thr-217) interacts with D2 via a hydrogen bond. A water bridge is formed through binding of Phe-275 to a water molecule and the water molecule forming a hydrogen bond interaction with Gln-185 and Glu-188, and compounds D2 and D7 forms a hydrogen bond with the water molecule. D9 also forms a hydrogen bond with Gln-185 as well as Glutamic acid-211 (Glu-211), which forms part of the hinge region. This hydrogen bond interaction between Glu-211 and D9 is an interaction seen in other docking studies as well<sup>113-114</sup>.

D3 and D6 interacts with arginine-137 (Arg-137) via a hydrogen bond, a protein-ligand interaction previously reported on<sup>114</sup>. Whereas D10 and D11 form a  $\pi$ -cation interaction with Arg-137, whereby the  $\pi$ -system of the aromatic rings of D10 and D11 interacts with the cationic Arg-137 sidechain. A  $\pi$ - $\pi$  stacking interaction occurs between D2 and D7 and Phe-144. A similar  $\pi$ - $\pi$  stacking interaction occurs between D4 and D9, and Phe-275. A hydrogen bond interaction is formed by compound D6 and D9 and Lys-141 an interaction that has been seen in other docking studies as well<sup>113</sup>. Another interaction that has been seen in other docking studies is the hydrogen bond interaction formed between compound D8 and Lys-162<sup>113</sup>. A novel  $\pi$ -cation interaction is formed by D4 and D5 with Lys-162. Asp-274 acts as a donor in the hydrogen bonding interaction between it and compound D4 and D9, an interaction reported on previously in docking studies<sup>113</sup>. In an interaction seen before between an AURKA inhibitor and Leu-139, D8 forms a hydrogen bond with Leu-139<sup>113</sup>. Proline-214 which forms part of the hinge region interacts with D6, D10, and D11 through a hydrogen bond interaction. The interactions with the hinge region residues seem to play a role in the successful binding of inhibitors into the ATP catalytic site<sup>114</sup>.

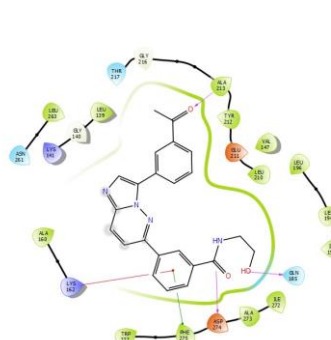
D2



D3

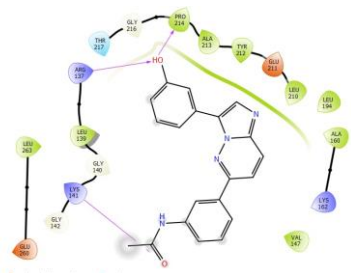


D4

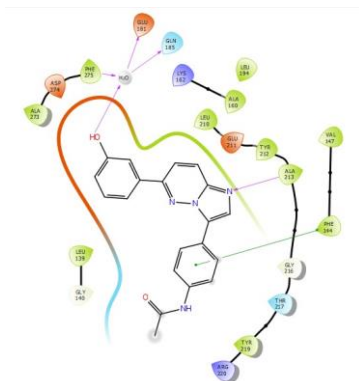


between D2 and Phe-144. A similar  $\pi$ - $\pi$  stacking interaction occurs between D4 and Phe-275. A hydrogen bond interaction is formed by compound D6 and Lys-141. A  $\pi$ -cation interaction is formed by D4 and D5 with Lys-162. Asp-274 forms a hydrogen bonding interaction with D4.

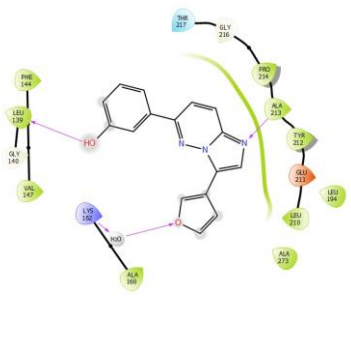
D6



D7



D8



D9

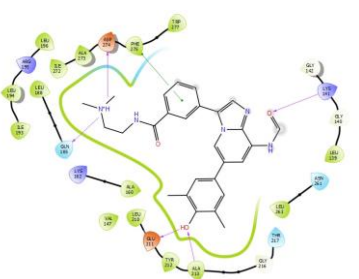


Figure 3. 6: Ligand-protein interaction diagram of D6-D9 complexed with AURKA. Compounds D7-D9 forms a hydrogen bond interaction with Ala-213. A water bridge is formed between Phe-275, Gln-185, Glu-188, and D7. D9 also forms a hydrogen bond with Gln-185 as well as Glu-211. D6 forms a hydrogen bond interaction with Arg-137. D7 forms a  $\pi$ - $\pi$  stacking interaction with Phe-144. A similar  $\pi$ - $\pi$  stacking interaction

occurs between D9 and Phe-275. A hydrogen bond interaction is formed by D9 and Lys-141. D8 forms a hydrogen bond interaction with Lys-162 and Leu-139. D9 forms a hydrogen bond interaction with Asp-274. D6 forms a hydrogen bond interaction with Pro-214

D10

D11

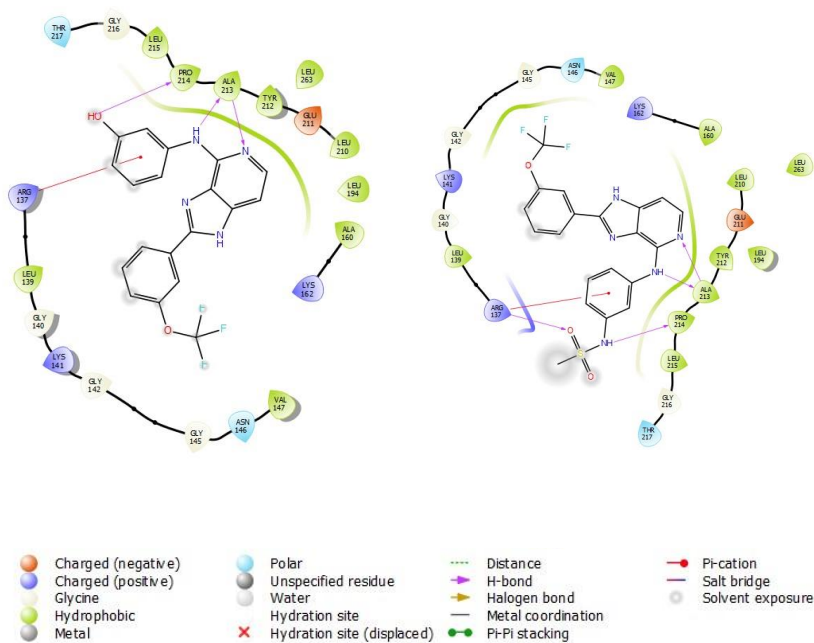


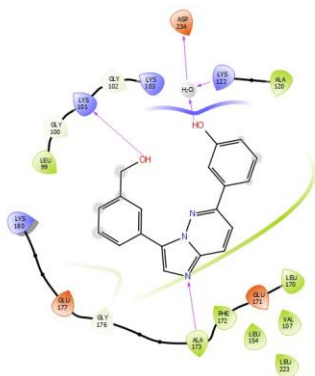
Figure 3. 7: Ligand-protein interaction diagram of D10-D11 complexed with AURKA. Compounds D10 and D11 forms a hydrogen bond interaction with Ala-213. D10 and D11 form a  $\pi$ -cation interaction with Arg-137. D10 and D11 forms a hydrogen bond interaction with Pro-214

### 3.1.3. AURKB protein-ligand interactions D2-D8

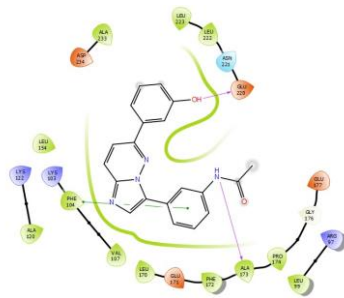
Like with AURKA, key residues within the AURKB hinge region play an important role in the binding of inhibitors into its catalytic site<sup>112,115</sup>. The hinge region usually includes a hydrogen donor (Ala-213 in AURKA) flanked by two hydrogen acceptors<sup>112,115</sup>. In AURKB the key residue is Ala-173, and hydrogen bonding interaction between this residue and an inhibitor seem to be the key indicator of its potential effectivity. From the ligand-protein interaction diagrams of compound D2-D8 with AURKB (Figure 3.8 and 3.9), compounds D2, D3, D4, D5, D7 and D8 forms hydrogen bond interactions with Ala-173. A water-bridge is formed between D2, Lys-122 and Asp-234, where D2 and Lys-122 acts as hydrogen bond donors, binding a water molecule water, and the water molecule acts as a hydrogen bond donor binding Asp-234. Hydrogen bond interactions between Lys-122 and AURKB inhibitors have previously been reported on, however a water-bridge hydrogen binding interaction of this kind seems to be a novel observation<sup>112</sup>. Hydrogen bonding interactions with Lys-101 is an interaction known from other docking studies<sup>112</sup>. Here D2 interact with Lys-101 via hydrogen bond interaction where the D2 hydroxyl group acts as a hydrogen bond donor. D2 and D6 forms a hydrogen bond with Asp-234 and Glu-177 forms hydrogen bond interactions with D7 and D8, interactions previously reported on with other inhibitors in docking studies<sup>112</sup>.

D4 and a water molecule form a hydrogen bond with Lys-103, where the D4 carbonyl oxygen acts as a hydrogen acceptor and Lys-103 the donor, water acts as a hydrogen bond donor between its interaction with Lys-103. D5 also forms a hydrogen bond with Lys-103. D4 and D5 forms a hydrogen bond with Lys-180 and D7 forms a hydrogen bond with Gln-145. Additional interactions are hydrogen bonds formed by D3 and D4 with Glu-220, and  $\pi$ - $\pi$  stacking interactions with Phe-104 and D3 and D6.

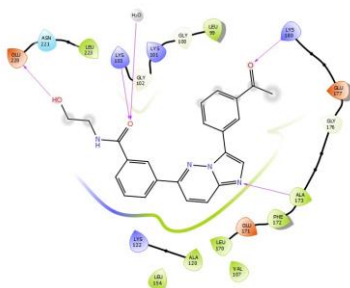
D2



D3



D4



D5

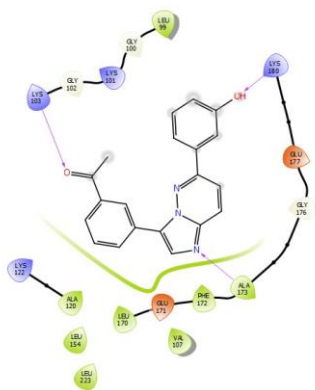
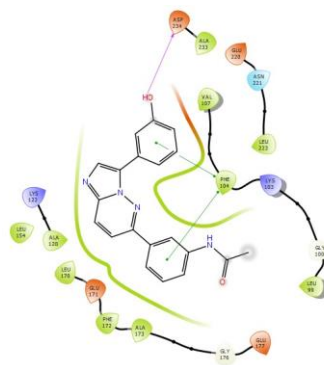


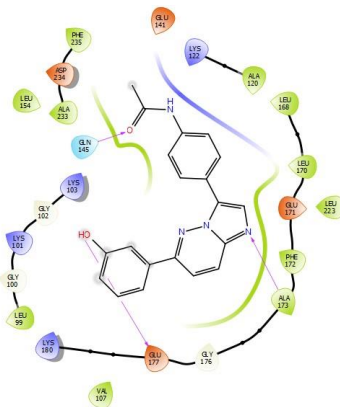
Figure 3. 8: Ligand-protein interaction diagram of D2-D5 complexed with AURKB. Compounds D2-D5 forms hydrogen bond interactions with Ala-173. A water-bridge is formed between D2, Lys-122 and Asp-234. D2 forms a hydrogen bond with Asp-234. D4 and a water molecule form a hydrogen bond with Lys-103. D5 also forms a hydrogen bond with Lys-103. D4 and D5 forms a hydrogen bond with Lys-180.

Additional interactions are hydrogen bonds formed by D3 and D4 with Glu-220, and  $\pi$ - $\pi$  stacking interactions with Phe-104 and D3.

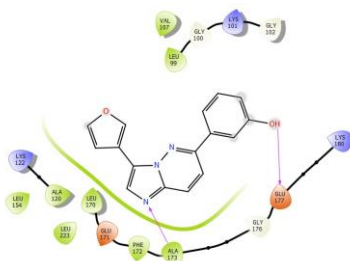
D6



D7



D8



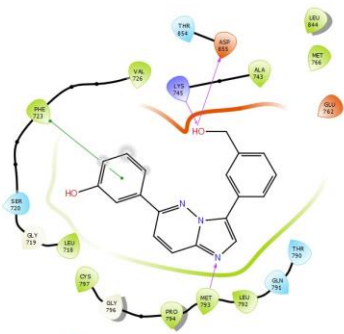
- |                    |                            |                    |                  |
|--------------------|----------------------------|--------------------|------------------|
| Charged (negative) | Polar                      | Distance           | Pi-cation        |
| Charged (positive) | Unspecified residue        | H-bond             | Salt bridge      |
| Glycine            | Water                      | Halogen bond       | Solvent exposure |
| Hydrophobic        | Hydration site             | Metal coordination |                  |
| Metal              | Hydration site (displaced) | Pi-Pi stacking     |                  |

Figure 3. 9: Ligand-protein interaction diagram of D6-D8 complexed with AURKB. compounds D5, D7 and D8 forms hydrogen bond interactions with Ala-173. D6 forms a hydrogen bond with Asp-234 and Glu-177 forms hydrogen bond interactions with D7 and D8. D6 forms a  $\pi$ - $\pi$  stacking interactions with Phe-104.

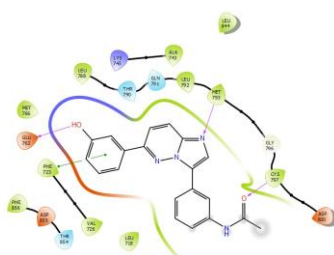
### 3.1.4. EGFR protein-ligand interactions D2-D7

Methionine-793 (Met-793) is an amino acid within the tyrosine-kinase (TK) domain of EGFR and seems to play an important role in the binding of EGFR-TK inhibitors, and its effectivity<sup>116-117</sup>. Met-793 play a role in molecular recognition of substrates in the TK binding pocket<sup>116-117</sup>. Another key residue within the TK domain of EGFR is Asp-800<sup>116-117</sup>. Compounds D2, D3, D4, D5, D6, and D7 all form hydrogen bond interactions with Met-793 (Figure 3.10 – 3.11). Compound D5 forms a hydrogen bond with the key Asp-800 residue. Phe-723, a residue found at the entrance of the TK active-site, interacts with D2-D4, D6 and D7 with via  $\pi$ - $\pi$  stacking<sup>117</sup>. Compound D6 has two  $\pi$ - $\pi$  stacking interactions between its aromatic side-groups and the aromatic sidechain of Phe-723. An important conserved interaction is the hydrogen bonding between D2 and Asp-855 and Lys-745<sup>117</sup>. Other hydrogen bond interactions observed are those of D3 and D7 with Glu-762, D3 with Cys-797 and D4 with Ser-720.

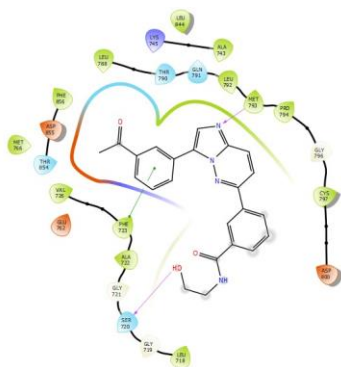
D2



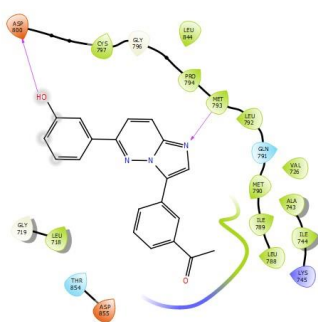
D3



D4



D5



Other hydrogen bond interactions observed are those of D3 with Glu-762 and Cys-797 and D4 with Ser-720.

D6

D7

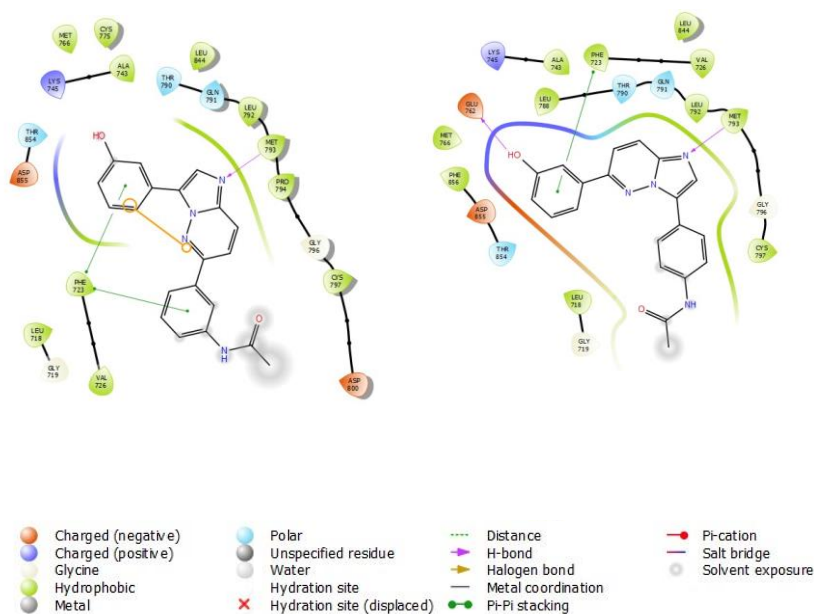


Figure 3. 11: Ligand-protein interaction diagram of D6-D7 complexed with EGFR. Compounds D6 and D7 form hydrogen bond interactions with Met-793. Phe-723 interacts with D6 and D7 with via  $\pi$ - $\pi$  stacking. Compound D6 has two  $\pi$ - $\pi$  stacking interactions with Phe-723. D7 forms a hydrogen bond interaction with Glu-762.

### 3.2. Results of the In vitro screening of compound D2-D11 with the CV viability assay

Screening of the lead compounds (D2-D11) in MDA-MB-231 cells using the CV assay showed that compounds D3- D11 had very little to no activity at the concentrations

they were tested at (Figure 3.12). It wasn't possible to calculate IC<sub>50</sub>s for compound D3-D11, because the viability of the cells never went below 80%.

### CV Lead Compounds D2-D11 Screening in MDA-MB-231

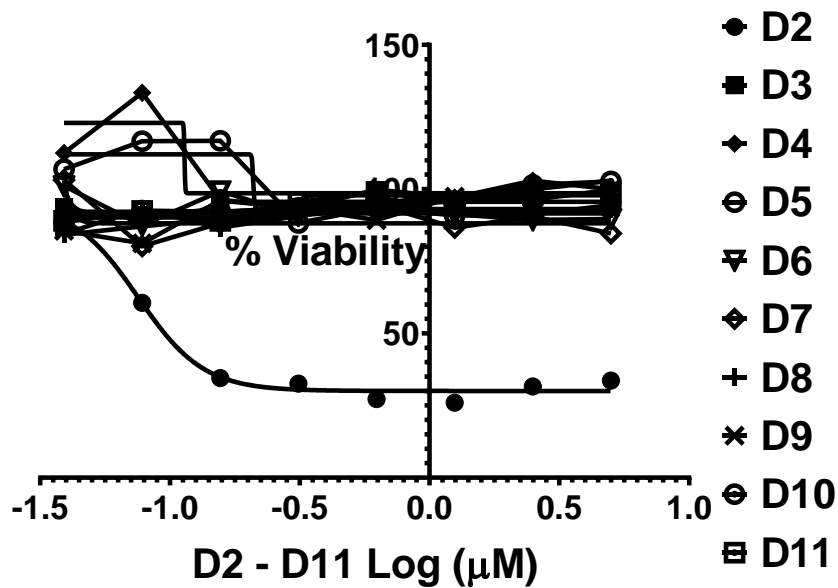


Figure 3. 12: Dose-response curve of compounds D2-D11 tested in MDA-MB-231 cells. The right-hand legend indicates which line style represents which compound.

Activity has however been observed in compound D2, from the dose-response curve it is clear that an increase in the concentration leads to a decrease in viability of the MDA-MB-231 cells. An IC<sub>50</sub> of D2 was calculated from the screening results and it is in the nanomolar range (table 3.3).

Table 3. 3: A list of the screening results of compound D2-D11. It was not possible to calculate IC<sub>50</sub> values for D3-D11.

Compound	IC <sub>50</sub> µM
D2	0.1739
D3	~> 5

D4	~> 5
D5	~> 5
D6	~> 5
D7	~> 5
D8	~> 5
D9	~> 5
D10	~> 5
D11	~> 5

### 3.3. MTT results

The single active compound, D2, from the list of 10 hit compounds from the HTVS was tested on MDA-MB-231 cells to calculate its  $IC_{50}$ . From the dose-response curve, as was the case with the CV screening, a clear dose dependant decrease in cell viability can be seen (Figure 3.13). The  $IC_{50}$  is calculated as 0.1968  $\mu$ M which means it falls within the nanomolar range. The coefficient of determination ( $R^2$ ), for the  $IC_{50}$  was calculated as  $R^2= 0.9911$ , that is the  $R^2 \geq 0.90$  and thus falls within accepted criteria for a linear regression model at 95% confidence interval and  $\Delta R \geq 0.1^{118}$ . The  $R^2$  value indicates that the data falls within the model (the fitted regression line) 99.11% of the time.

### MTT Dose Response Curve of D2 Treated MDA-MB-231

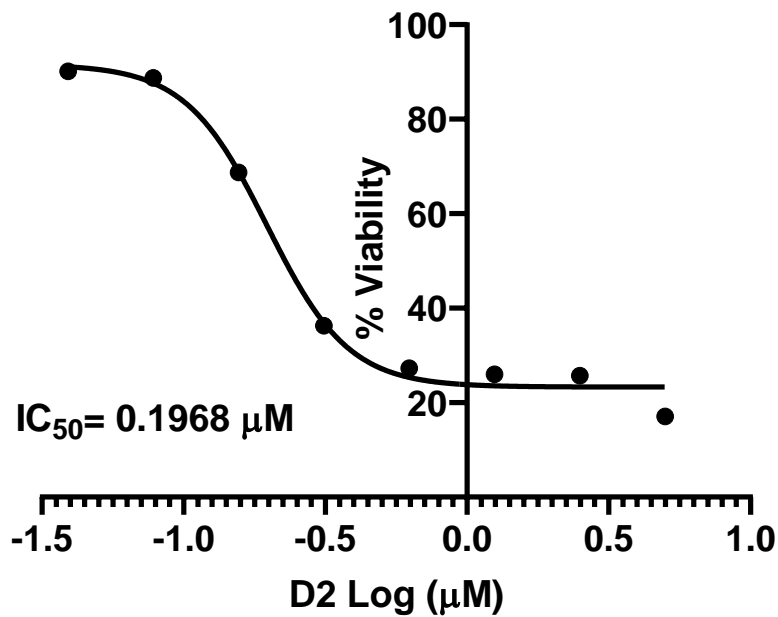


Figure 3. 13: The dose response curve of the MDA-MB-231 cells after 48 h treatment with D2, determined with the MTT assay. The IC<sub>50</sub> of 0.1968 µM is indicated on the graph. A non-linear regression curve fit was performed to estimate the IC<sub>50</sub>. This experiment was performed in triplicate with three biological repeats.

Based on the results of the MTT assay, there is no significant difference in viability between the vehicle control (0.1% DMSO v/v in CCM), (1.158 OD ± 0.1292 OD) and the CCM only (1.174 OD ± 0,1044) controls (Figure 3.14), based upon the Welch's t-test (p>0.9999). Based on this, any future experimentation can be performed with only a vehicle control and not both a vehicle and CCM control.

### Control vs Vehicle Control in MDA-MB-231 cells

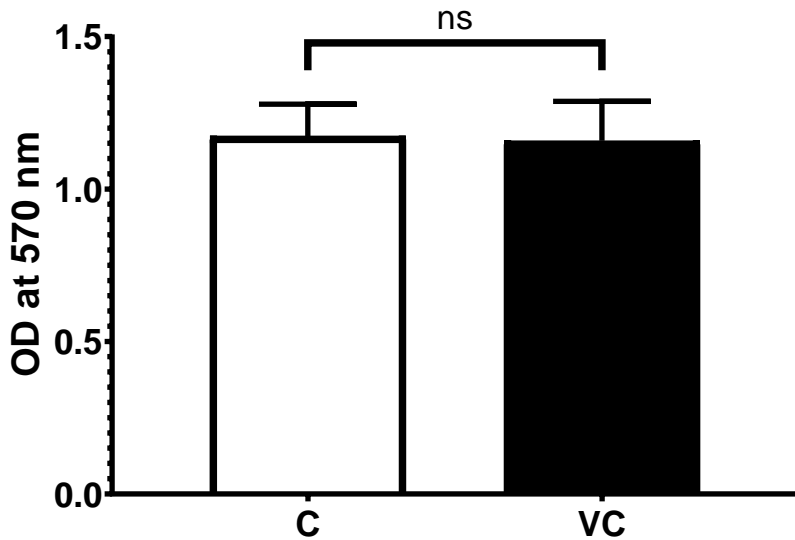


Figure 3. 14: A bar chart comparing the MTT assay ODs of the control (C) and vehicle control (VC). Error bars indicate the standard deviation from the mean (Std of C= 0.1044; Std of VC= 0.1292). No significant difference was found between C and VC cells (Welch's t-test  $p > 0.9999$ ). OD: optical density at 570 nm. This experiment was performed in triplicate with three biological repeats.

Next, the EA.hy926 cells were treated with the  $IC_{50}$  of D2 calculated from the MTT assay of the MDA-MB-231 cells. The EA.hy926 treatment followed the same basic procedure of 5000 cells per well, but instead of a treatment range, cells were only treated with the  $IC_{50}$  and a vehicle control was also included (and not a CCM only control). From Figure 3.15 it is clear that D2 treatment with the MDA-MB-231  $IC_{50}$  does not have a significant effect ( $p=0.9862$ ) on EA.hy926 viability ( $1.616 \text{ OD} \pm 0.1751 \text{ OD}$ ) relative to the VC ( $1.583 \text{ OD} \pm 0.3561 \text{ OD}$ ).

### Effect of the D2 IC<sub>50</sub> in EA.hy926 cells

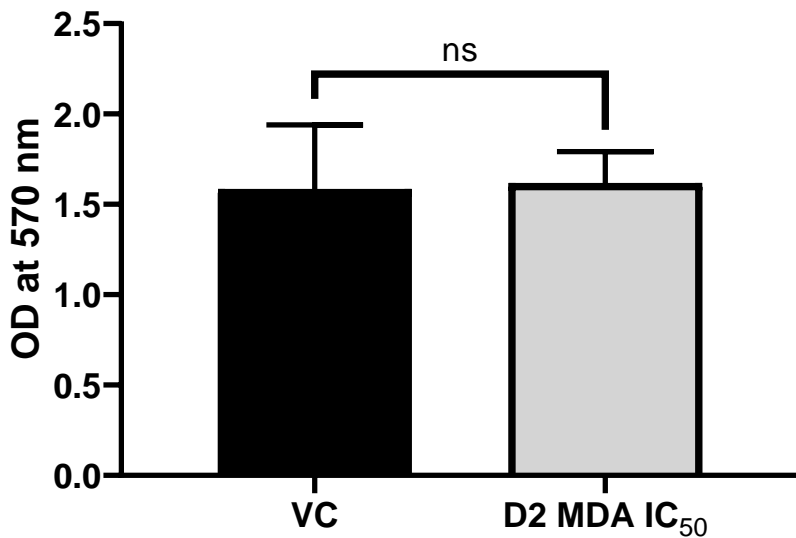


Figure 3. 15: Bar graph comparing the effect of the MDA-MB-231 IC<sub>50</sub> of D2 on EA.hy926 cells. Error bars indicate standard deviation from the mean (Std VC= 0.3561; Std D2 IC<sub>50</sub>= 0.1751). No significance was found between VC and D2 MDA IC<sub>50</sub> treated EA.hy926 cells (Welch's t-test p= 0,9862). OD: optical density at 570 nm. This experiment was performed in triplicate with three biological repeats.

#### 3.4. Results of the analysis of the *in vitro* effect of D2

The *in silico* results and cytotoxic effect of D2 observed in the *in vitro* screening and the IC<sub>50</sub> calculated from the MTT, pointed to efficacy as an inhibitor, warranting further investigation, the results of which follows here.

##### 3.4.1. BRD4 and AURKA ELISA

The anti-BRD4 ELISA results indicate that there is expression of BRD4 in both MDA-MB-231 and EA.hy926 cells, thus D2 should theoretically be able to bind to BRD4 and inhibit its function. The EA.hy926 cells seem to express more BRD4 than the MDA-MB-231 cells (Figure 3.16).

In the MDA-MB-231 VC cells, the mean concentration of BRD4, as interpolated from the standard curve, is 413.20 ng/l ± 35.33 ng/ l and the mean concentration of the D2-treated cells is 335.30 ng/l ± 53.80 ng/ l. The decrease in BRD4 expression in D2

treated cells compared to the VC is statistically significant ( $p=0.0030$ ). The EA.hy926 cells on the other hand showed a significant increase ( $p=0.0133$ ) in the concentration of BRD4 in the D2-treated cells ( $532.50 \text{ ng/l} \pm 65.99 \text{ ng/l}$ ) compared to the VC ( $464.04 \text{ ng/l} \pm 20.97 \text{ ng/l}$ ).

### Interpolated concentrations of BRD4 in MDA-MB-231 and EA.hy926 cells

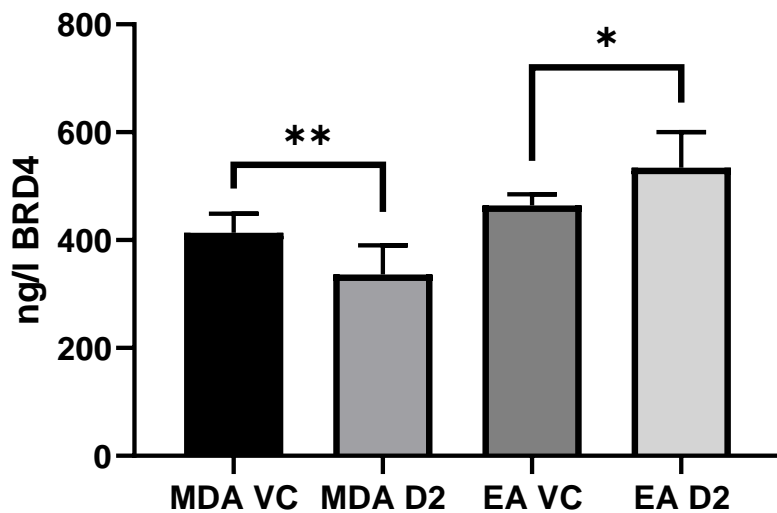


Figure 3. 16: Bar chart of the interpolated concentrations of BRD4 in the VC and D2 treated MDA-MB-231 and EA.hy926 cells. Error bars indicate the Std dev. Significance in differences between the VC vs D2 treatment in each cell line is indicated with asterisks (\*  $p<0.05$ ; \*\*  $p<0.01$ ; \*\*\*  $p<0.005$ ; \*\*\*\*  $p<0.0001$ ). MDA VC vs MDA D2 ( $p=0.0030$ ), EA VC vs EA D2 ( $p=0.0133$ ). This experiment was performed in triplicate with three biological repeats.

From the anti-AURKA ELISA it is clear that both cell lines do express AURKA. Here MDA-MB-231 cells seem to express more AURKA than do the EA.hy926 cells.

The VC treated MDA-MB-231 cells (Figure 3.17) have a mean AURKA concentration of  $3.79 \text{ ng/ml} \pm 0.2752 \text{ ng/ml}$ , and the D2-treated cells that have an AURKA concentration ( $3.41 \text{ ng/ml} \pm 0.4226 \text{ ng/ml}$ ) significantly lower than the VC ( $p=0.0431$ ). The concentration of AURKA in the VC treated EA.hy926 cells ( $2.96 \text{ ng/ml} \pm 0.3315$

ng/ ml) was not different than that of the D2 treated cells (mean concentration: 3.11 ng/ ml  $\pm$  0.6043 ng/ ml).

### Interpolated concentrations of AURKA in MDA-MB-231 and EA.hy926 cells

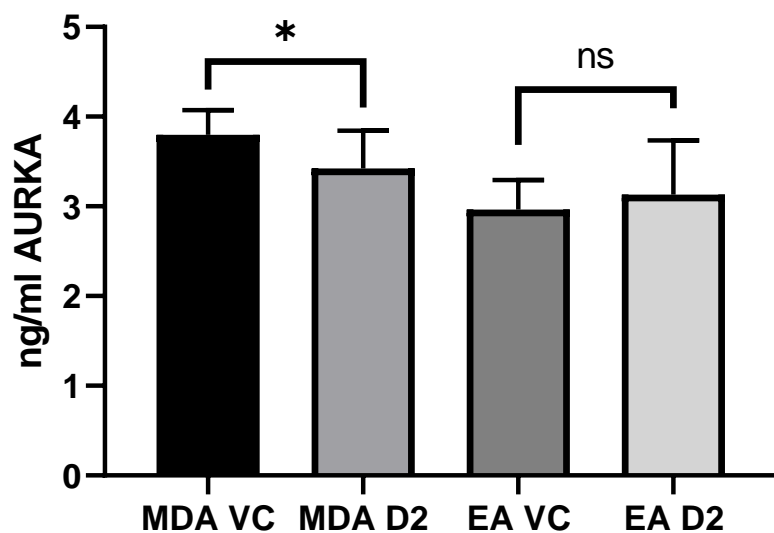


Figure 3. 17: Bar chart of the interpolated concentrations of AURKA in the VC and D2 treated MDA-MB-231 and EA.hy926 cells. Error bars indicate the Std dev. Significance in differences between the VC vs D2 treatment in each cell line is indicated with asterisks (\*  $p < 0.05$ ; \*\*  $p < 0.01$ ; \*\*\*  $p < 0.005$ ; \*\*\*\*  $p < 0.0001$ ). MDA VC vs MDA D2 ( $p = 0.0431$ ), EA VC vs EA D2 ( $p = 0.4821$ ). This experiment was performed in triplicate with three biological repeats.

#### 3.4.2. The effect of D2 on the cell cycle

To analyse the effect of the D2  $IC_{50}$  on the cell cycle, flow cytometry was employed.

Using the Muse specific Cell Cycle Analysis kit, the effect of D2 was elucidated. From the representative histograms (Figure 3.18), there is no difference in the number of MDA-MB-231 cells in the G0/G1 phase when treated with the D2  $IC_{50}$  compared to the VC. There is however a decrease in the number of cells in S-phase indicating towards a potential block that prevents the cells from progressing to S-phase.

Statistical analysis of the results (Figure 3.20) indicated no significant difference between the amount of VC treated cells ( $70.78\% \pm 0.3663\%$ ) and D2 treated ( $72.69\% \pm 2.381\%$ ) cells in G0/G1-phase ( $p=0.0587$ ). A significant difference in the number of cells in S-phase was noted between VC and D2 ( $p=0.0093$ ), where the amount of D2 treated cells ( $7.804\% \pm 0.5766\%$ ) in S-phase was decreased, relative to the VC ( $8.903\% \pm 0.4770\%$ ). No significant difference ( $p=0.5609$ ) was observed in the cell numbers in the G2/M-phase between VC treated cells ( $19.76\% \pm 1.030\%$ ) and the D2 treated cells ( $19.24\% \pm 1.963\%$ ). NOC had a significant effect on each phase of the cell cycle relative to the vehicle control ( $p<0.05$ ). In G0/G1 were  $47.08\% \pm 2.226\%$  of the cells. In S-phase it was  $14.24\% \pm 1.485\%$  of the cells. And a significant accumulation of NOC treated cells in G2/M ( $37,40\% \pm 0,9823\%$ ) is indicative of a G2/M block (a known effect of NOC).

The cell cycle analysis of the EA.hy926 cells treated with the  $IC_{50}$  of D2, as calculated in the MDA-MB-231 cells (Figure 3.19 and 3.21), showed no significant difference ( $p=0,3685$ ) in the number of cells in G0/G1-phase between the D2 ( $65.07\% \pm 1.225\%$ ) and VC-treated cells ( $63.95\% \pm 1.913\%$ ). There was a significant difference between the cell number of VC and D2-treated cells in S-phase ( $p=0.0003$ ), with the D2-treated cell number ( $11.93\% \pm 1.913\%$ ) being higher than that of the VC ( $8.443 \pm 0.3597\%$ ). The difference in the number of cells in G2/M-phase between VC ( $27.39\% \pm 0.8161\%$ ) and D2-treated cells ( $22.76\% \pm 1.736\%$ ) were significant ( $p=0.0072$ ). Analysis of the VC versus the NOC positive control showed no significant difference ( $p=0.1301$ ) between cell numbers in G0/G1 ( $61.98\% \pm 0.8144\%$ ). A significant difference ( $p<0.0001$ ) in the cell numbers in S-phase between VC and NOC ( $11.48\% \pm 0.2381\%$ ). The number of cells in G2/M-phase between VC and NOC ( $25.40\% \pm 0.9789\%$ ) was significantly decreased ( $p=0.0214$ ).

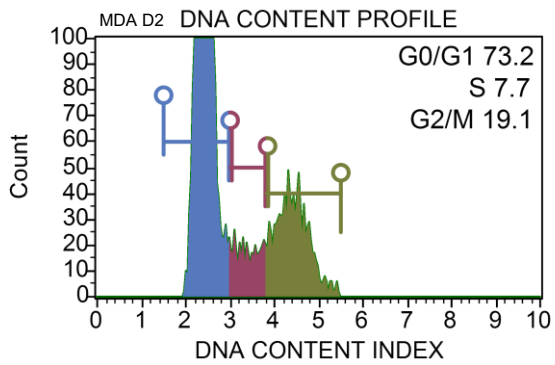
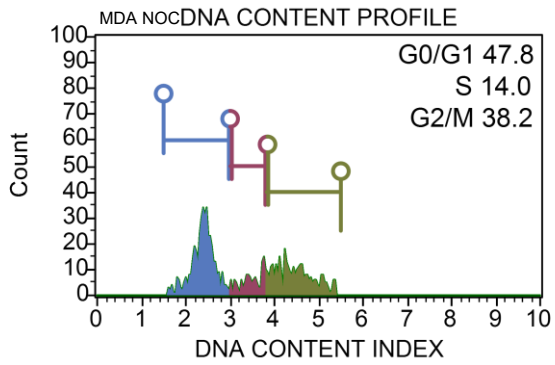
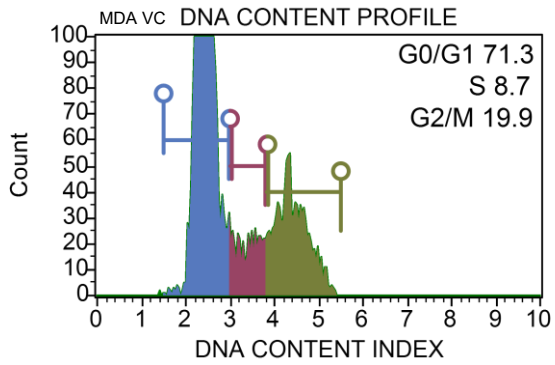


Figure 3. 18: Representative histograms of the DNA content vs the cell count percentage of MDA-MB-231 cells, chosen from three biological repeats to best represent the data. Graphs are marked as MDA VC, MDA NOC, and MDA D2 to indicate the treatment conditions. This experiment was performed in triplicate with three biological repeats.

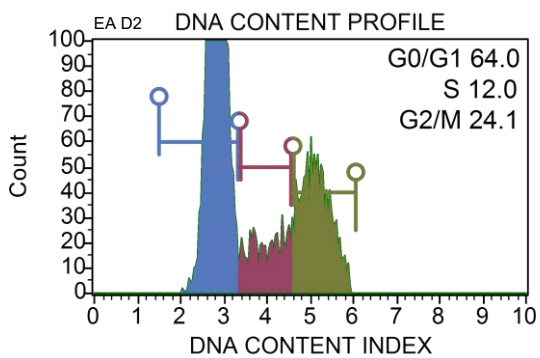
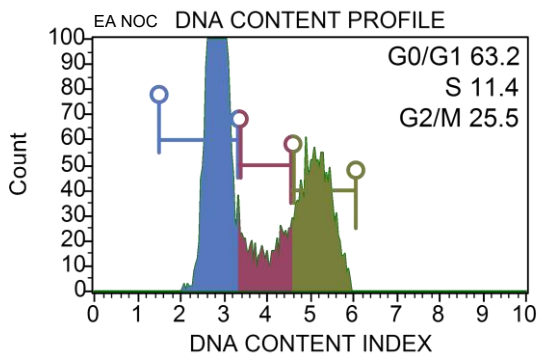
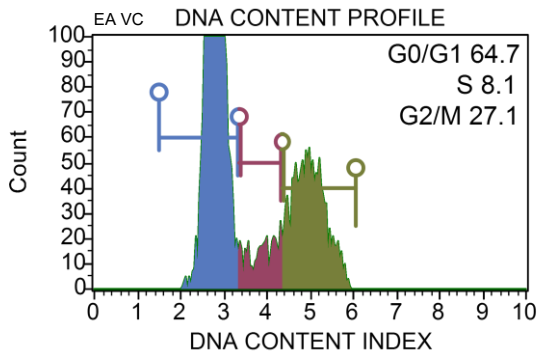


Figure 3. 19: Representative histograms of the DNA content vs the cell count percentage of EA.hy926 cells, chosen from three biological repeats to best represent the data. Graphs are marked as EA VC,

EA NOC, and EA D2 to indicate the treatment conditions. This experiment was performed in triplicate with three biological repeats.

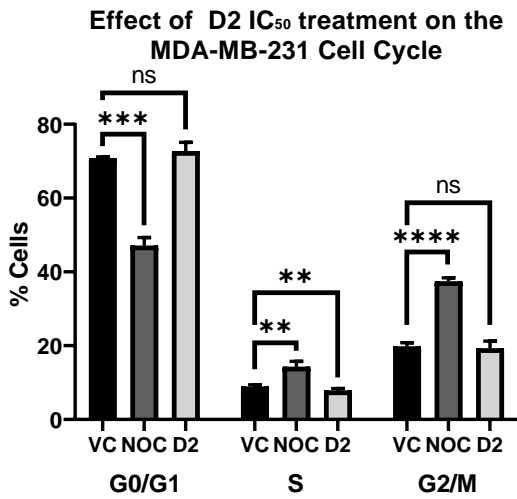


Figure 3. 20: Bar graph of MDA-MB-231 cells in the different cell cycles after treatment with the D2 IC<sub>50</sub>. Each bar represents three technical repeats from three biological repeats. Each treatment within a cell cycle phase is contrasted with the VC. Error bars indicate the standard deviation from the mean. Welch's t-test was performed to compare each treatment condition with the VC. G0/G1: VC vs NOC ( $p=0.0002$ ), VC vs D2 ( $p=0.0587$ ); S: VC vs NOC ( $p=0.0034$ ), VC vs D2 ( $p=0.0093$ ), VC vs D2 ( $p=0.0003$ ); G2/M: VC vs NOC ( $p<0.0001$ ), VC vs D2 ( $p=0.5609$ ). This experiment was performed in triplicate with three biological repeats.

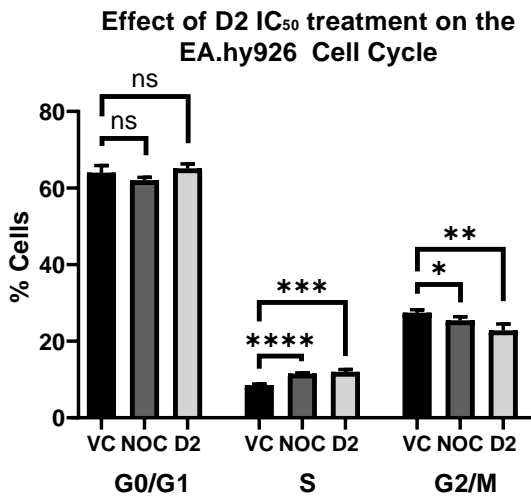


Figure 3. 21: Bar graph of EA.hy926 cells in the different cell cycles after treatment with the D2 IC<sub>50</sub> of the MDA-MB-231 cells. Each treatment within a cell cycle phase is contrasted with the VC. Error bars indicate the standard deviation from the mean. Welch's t-test was performed to compare each treatment condition with the VC. G0/G1: VC vs NOC ( $p=0.1301$ ), VC vs D2 ( $p=0.3685$ ); S: VC vs NOC ( $p<0.0001$ ), VC vs D2 ( $p=0.0003$ ); G2/M: VC vs NOC ( $p=0.0214$ ), VC vs D2 ( $p=0.0072$ ). This experiment was performed in triplicate with three biological repeats.

### 3.5. Results of the investigation into ROS and apoptosis in D2 treated cells

Analysis of BRD4 and AURKA expression, in conjunction with the analysis of the effect of D2 on the cell cycle shed some light on the activity of D2. But it did not adequately explain the cytotoxicity observed. Thus additional investigation into the effect of D2 in MDA-MB-231 and EA.hy926 cells followed.

#### 3.5.1. Intracellular ROS

The MDA.MB-231 and EA.hy926 cells were treated with the D2 IC<sub>50</sub>, with the VC as reference and NOC as positive control. DHE, a stain that is reduced to the fluorochrome EB by superoxide radicals and which intercalates into DNA serving as an indicator of intracellular ROS, were used to quantify oxidative burden of the treated cells.

From the histograms and statistical analysis (Figure 3.22 and 3.24) of the MDA-MB-231 a marked increase in ROS+ cells between the VC (17.94 %  $\pm$  2.676 %) and D2

treated cells ( $57.70\% \pm 2.294\%$ ) can be observed. The ROS profiles of D2 indicates increased ROS even compared to the NOC positive control ( $40.54\% \pm 0.9982\%$ ). In terms of ROS- cells, there was a decrease in the amount of D2-treated cells ( $41.92\% \pm 2.222\%$ ) relative to the VC ( $81.33\% \pm 2.519\%$ ). A decrease in ROS- cells in the NOC treatment group ( $59.00\% \pm 0.8940\%$ ) relative to the VC was also observed.

Statistical analysis of the ROS profiles of the MDA-MB-231 cells indicate significant increases in ROS+ ( $p < 0.0001$ ) D2 treated cells relative to the VC (Figure 3.24). A significant decrease in ROS- cells were observed in the D2 treated cells relative to the VC ( $p < 0.0001$ ). The NOC positive control had a significant decrease in ROS- cells ( $p = 0.0001$ ) as well as a significant increase in ROS+ cells ( $p = 0.0001$ ) relative to the VC.

The EA.hy926 cells treated with the D2  $IC_{50}$  showed an increase ( $24.04\% \pm 1.580\%$ ) in ROS+ cells relative to the VC cells ( $16.29\% \pm 2.379\%$ ) as seen in Figure 3.23. The amount of ROS- cells in D2 ( $75.92\% \pm 1.567\%$ ) was decreased relative to the VC ( $83.61\% \pm 2.353\%$ ).

Statistical analysis (Figure 3.25) indicated that there was a significant decrease in ROS- cells in the D2 treatment group relative to the VC ( $p = 0.0035$ ) and a significant increase in ROS+ cells of the D2 treatment group relative to the VC ( $p = 0.0035$ ).

The amount of ROS+ cells in the NOC treatment group ( $37.12\% \pm 1.141\%$ ) also increased significantly relative to the VC ( $p < 0.0001$ ). And the amount of ROS- cells in the NOC treatment group ( $62.93\% \pm 1.085\%$ ) also decreased significantly relative to the VC ( $p = 0.0001$ ).

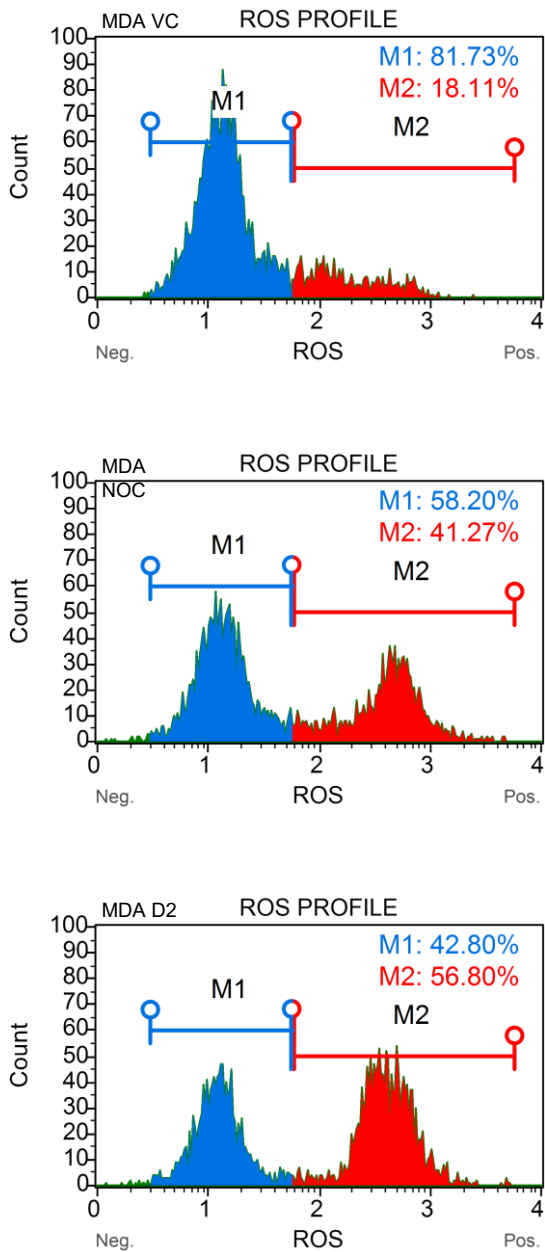


Figure 3. 22: Representative histograms of the different cell populations (M1: ROS- and M2: ROS+) within MDA-MB-231 cells after treatment with the D2 IC<sub>50</sub>, chosen from three biological repeats to best represent the data. Graphs are marked as MDA VC, MDA NOC, and MDA D2 to indicate the treatment conditions. This experiment was performed in triplicate with three biological repeats.

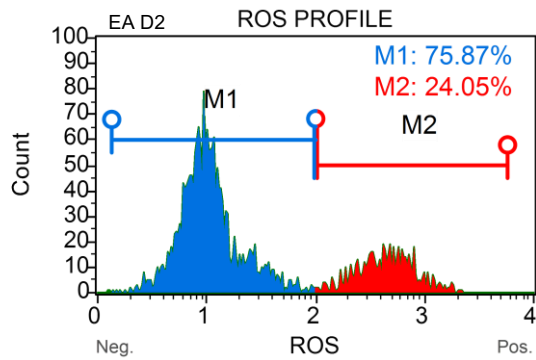
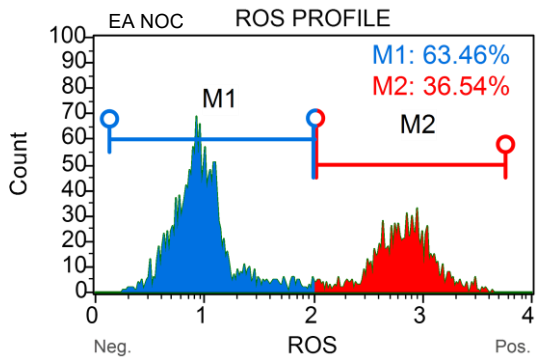
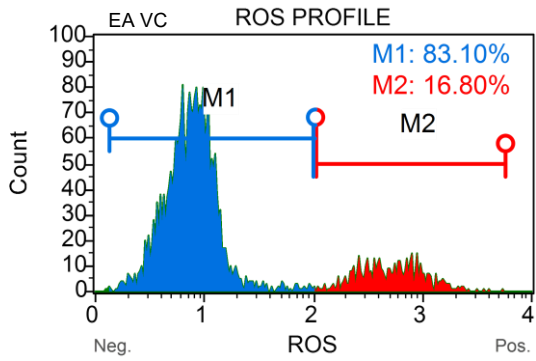


Figure 3. 23: Representative histograms of the different cell populations (M1: ROS- and M2: ROS+) within EA.hy926 cells after treatment with the D2 IC<sub>50</sub>, chosen from three biological repeats to best represent the data. Graphs are marked as EA VC, EA NOC, and EA D2 to indicate the treatment conditions. This experiment was performed in triplicate with three biological repeats.

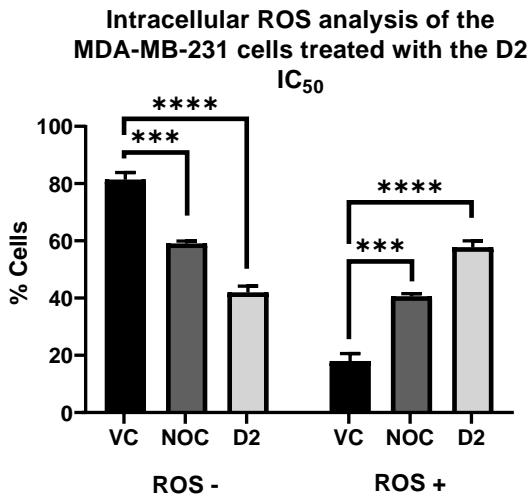


Figure 3. 24: Bar graph indicating the amount of ROS- and ROS+ cells in each treatment group, VC, NOC positive control, and D2 treated MDA-MB-231 cells. Error bars indicate the standard deviation from the mean. Welch's t-test was performed to compare each treatment condition with the VC. ROS-: VC vs. NOC  $p=0.0001$ ; VC vs. D2  $p<0.0001$ . ROS+: VC vs. NOC  $p=0.0001$ ; VC vs. D2  $p<0.0001$ . This experiment was performed in triplicate with three biological repeats.

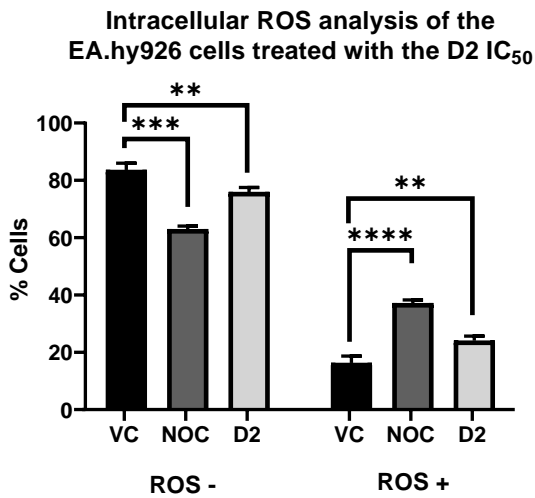
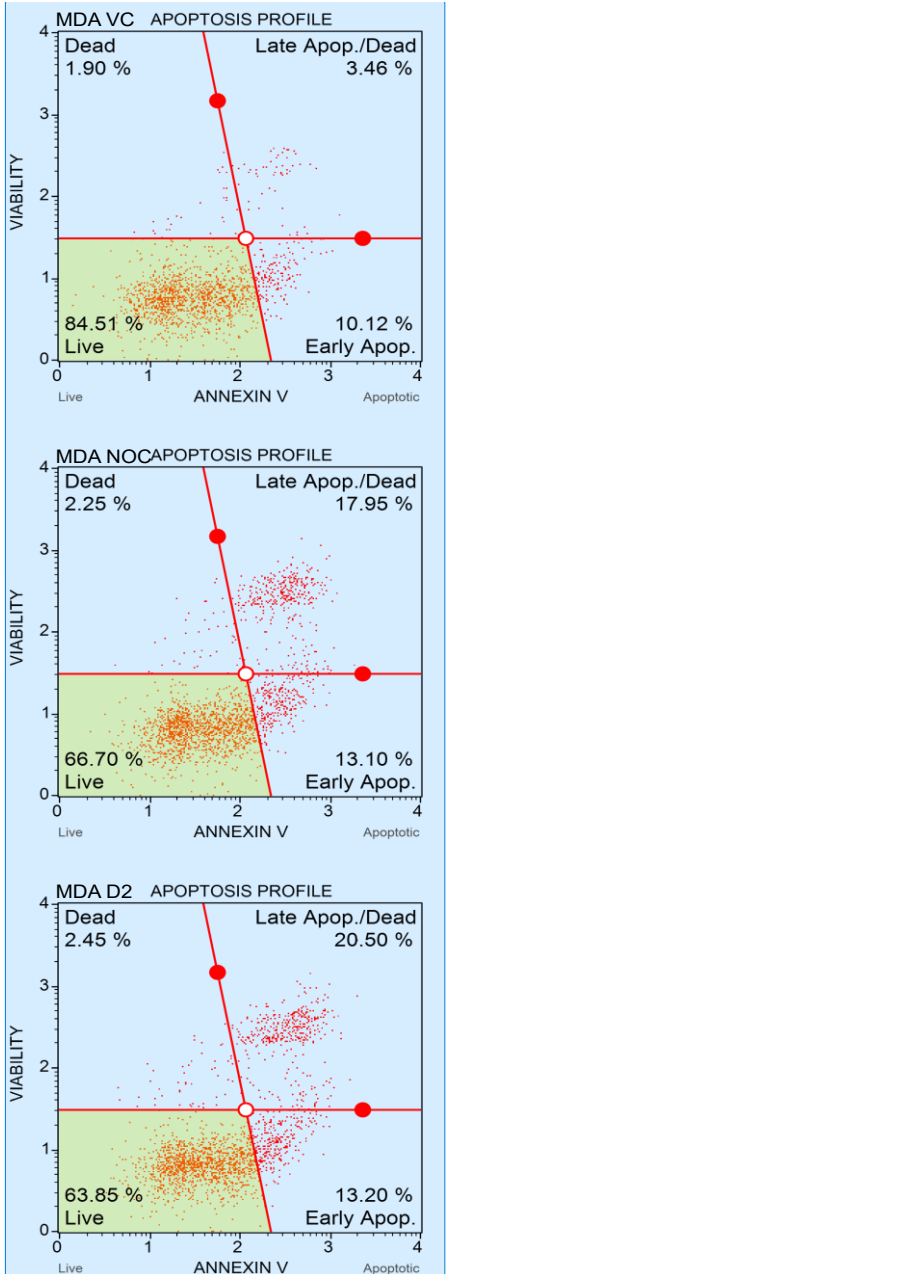


Figure 3. 25: Bar graph indicating the amount of ROS- and ROS+ cells in each treatment group, VC, NOC positive control, and D2 treated EA.hy926 cells. Error bars indicate the standard deviation from the mean. Welch's t-test was performed to compare each treatment condition with the VC. ROS-: VC vs. NOC  $p=0.0001$ ; VC vs. D2  $p=0.0035$ . ROS+: VC vs. NOC  $p<0.0001$ ; VC vs. D2  $p=0.0035$ . This experiment was performed in triplicate with three biological repeats.

### 3.5.2. Results of Annexin-V flow cytometry assay

From the apoptosis profiles (Figure 3.26) of the MDA-MB-231 cells under different treatment conditions (VC, NOC, and D2) a clear shift from living to apoptotic cells is visible. Analysis of the apoptotic profiles (Figure 3.28) confirms a significant decrease ( $p < 0.0001$ ) in the number of living cells in the NOC treatment ( $65.89 \% \pm 4.546 \%$ ), a significant increase ( $p < 0.0001$ ) in apoptotic cells ( $31.10 \% \pm 6.149 \%$ ), and, unexpectedly, no significant change ( $p = 0.0568$ ) in the number of dead cells ( $3.033 \% \pm 1.977 \%$ ) in the NOC treated control, relative to the VC. Looking at the D2 treated cells, the number of living cells ( $63.36 \% \pm 0.7395 \%$ ) decreased significantly ( $p < 0.0001$ ) relative to the VC ( $84.06 \% \pm 2.809 \%$ ). The number of apoptotic cells ( $34.82 \% \pm 0.9593 \%$ ) also increased significantly ( $p < 0.0001$ ) versus the VC ( $14.37 \% \pm 2.438 \%$ ), there however was no significant difference ( $p = 0.6986$ ) in the number of dead cells ( $1.833 \% \pm 0.3658 \%$ ) relative to the VC ( $1.640 \% \pm 1.862 \%$ ).

Treatment of the EA.hy926 cells with the D2  $IC_{50}$  caused a slight decrease (Figure 3.27) in the amount of living cells relative to the VC. Statistical analysis (Figure 3.29) indicated significant decrease ( $p = 0.0380$ ) between the number of live cells in D2 ( $83.63 \% \pm 0.9105 \%$ ) compared to the VC ( $84.40 \% \pm 0.7089 \%$ ). There was no significant difference ( $p = 0.0802$ ) in the number of apoptotic cells in D2 ( $11.31 \% \pm 0.9078 \%$ ) compared to the VC ( $11.89 \% \pm 0.5689 \%$ ). There was however a significant increase ( $p < 0.0001$ ) in the number of dead cells in D2 ( $5.092 \% \pm 0.8311 \%$ ) compared to the VC ( $3.722 \% \pm 0.4868 \%$ ). The positive control, as expected, showed a significant ( $p < 0.0001$ ) decline in live cells ( $64.73 \% \pm 1.108 \%$ ), and a significant increase ( $p < 0.0001$ ) in apoptotic cells ( $28.96 \% \pm 1.503 \%$ ) as well as a significant increase ( $p = 0.0003$ ) in dead cells ( $6.356 \% \pm 1.397 \%$ ) relative to the VC.



Commented [A4]: Change the title on the y-axis to 7-AAD

Figure 3. 26: Representative apoptosis profile of the MDA-MB-231 cells treated with IC<sub>50</sub> of D2, chosen from three biological repeats to best represent the data. Treatment conditions are displayed at the top left of each graph (MDA VC, MDA NOC, MDA D2). This experiment was performed in triplicate with three biological repeats.

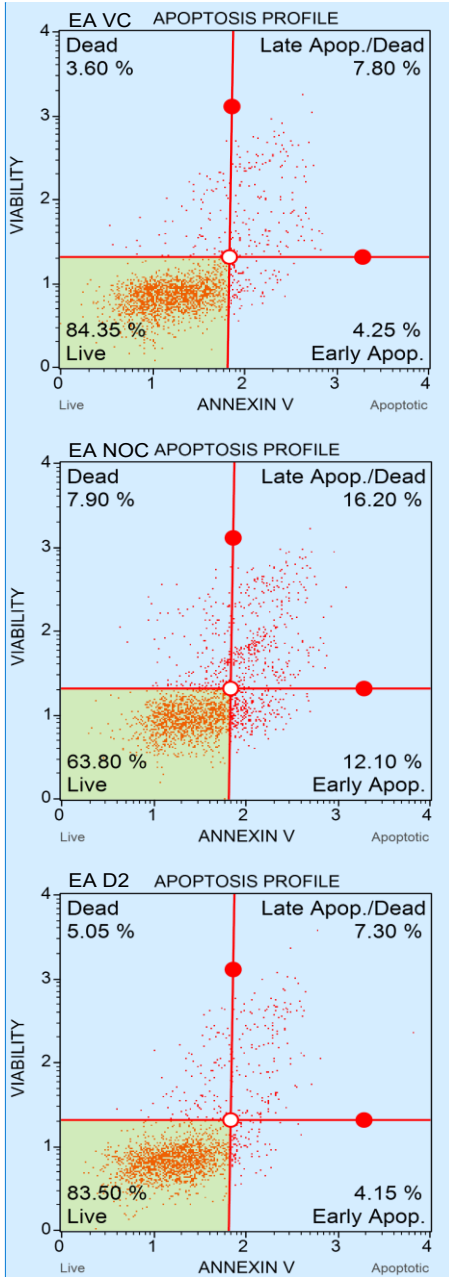


Figure 3. 27: Representative apoptosis profile of the EA.hy926 cells treated with IC<sub>50</sub> of D2 chosen from three biological repeats to best represent the data. Treatment conditions are displayed at the top left of each graph (EA VC, EA NOC, EA D2). This experiment was performed in triplicate with three biological repeats.

Commented [A5]: Change the title on the y-axis to 7-AAD

### Annexin V analysis of the MDA-MB-231 cells treated with the D2 IC<sub>50</sub>

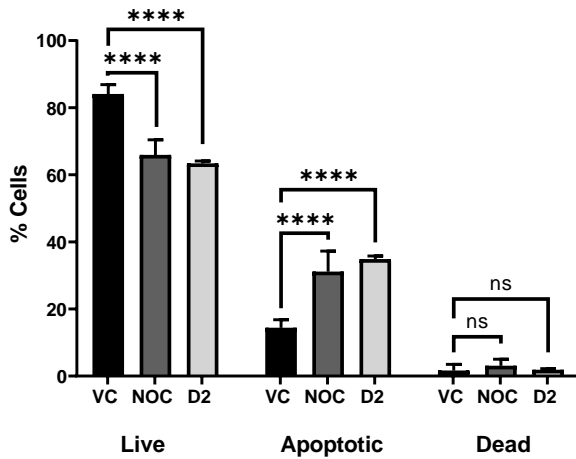


Figure 3. 28: Bar graph of the results of the Annexin-V flow cytometry of MDA-MB-231 cells. . Error bars indicate the standard deviation from the mean. Welch's t-test was performed to compare each treatment condition with the VC. Live cells: VC vs NOC  $p < 0.0001$ ; VC vs D2  $p < 0.0001$ . Apoptotic cells: VC vs NOC  $p < 0.0001$ ; VC vs D2  $p < 0.0001$ . Dead cells: VC vs NOC  $p = 0.0568$ ; VC vs D2  $p = 0.6986$ . This experiment was performed in triplicate with three biological repeats.

### EA.hy926 D2 IC<sub>50</sub> Annexin V

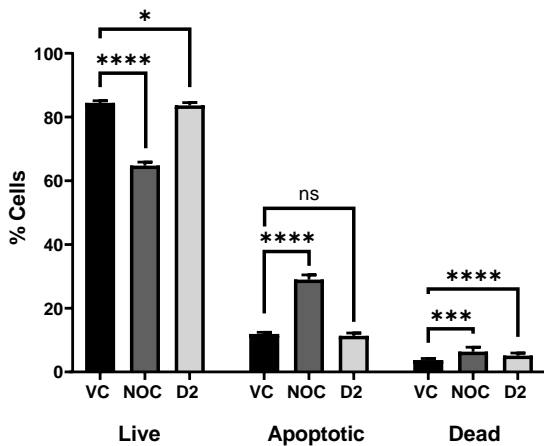


Figure 3. 29: Bar graph of the results of the Annexin-V flow cytometry of the EA.hy926 cells. . Error bars indicate the standard deviation from the mean. Welch's t-test was performed to compare each treatment condition with the VC. Live cells: VC vs NOC  $p < 0.0001$ ; VC vs D2  $p = 0.0380$ . Apoptotic cells: VC vs

NOC  $p < 0.0001$ ; VC vs D2  $p = 0.0802$ . Dead cells: VC vs NOC  $p = 0.0003$ ; VC vs D2  $p < 0.0001$ . This experiment was performed in triplicate with three biological repeats.

## 4. Discussion

The HTVS of the Biofocus library of compounds, containing 20 000 unique compounds, against BRD4, AURKA, AURKB, PLK1, and EGFR yielded some 10 hits for BRD4 and AURKA (D2-D11), 7 hits for AURKB (D2-D8), 6 hits for EGFR (D2-D7) and zero hits for PLK1. Interestingly all 10 of the compounds interacted favourably with the BD1 active site of BRD4. All 10 compounds formed hydrogen bond interactions with the highly conserved and very important Asn-140 residue of the BC loop. But from the *in vitro* screening only D2, also known as (3-{3-[3-(hydroxymethyl)phenyl]imidazo[1,2-b]pyridazin-6-yl}phenol) shows activity at relatively low concentrations. Compound D2 formed particularly favourable interactions with key residues of the BD1 BRD4. Notwithstanding the hydrogen bonding interaction of D2 with Asn-140, where the hydroxyl group of the phenol sidechain of D2 acts as the donor for the carboxamide oxygen of Asn-140. D2 interacts with 2 additional residues within the BD1 acetyl-lysine binding pocket, it forms a  $\pi$ - $\pi$  stacking interaction with Trp-81 (part of the WPF shelf), forming a T-shaped  $\pi$  interaction, where the positively charged framework of the aromatic ring of Trp81 interacts with the  $\pi$  electron cloud of the aromatic imidazo-group of D2. Lys-91, a ZA loop residue, interacts with D2 to form a hydrogen bond by means of the hydroxyl group of the benzyl alcohol sidechain of D2 that act as the hydrogen bond acceptor and the protonated lysyl sidechain of Lys-91 acting as the hydrogen bond donor<sup>119-120</sup>. The hydrogen bond between D2 and Asn-140 is a proven key interaction for BRD4 BD1 inhibitors<sup>109,121</sup>. As well as the additional stabilizing interactions with the ZA loop residue Lys-91, and the WPF shelf residue Trp-81, identifies D2 as a strong candidate as a BRD4 inhibitor<sup>81,109,121-122</sup>.

Perusing the docking results of AURKA, one would expect highly favourable screening results. But inspection of the protein-ligand interactions points to something else. The most important interaction to consider when screening for AURKA inhibitors of the catalytic site of the ATP binding pocket, is the interaction between the potential ligand and the Ala-213 residue<sup>112,114</sup>. The ligand must act dominantly with Ala-213 via a

hydrogen bond interaction, otherwise it will not bind stably, and no inhibition will take place<sup>112,114</sup>. Taking this into account it is clear that compounds D3 and D6 would definitely not have shown any activity with regards to AURKA inhibition due to their lack of Ala-213 ([Figure 3.2 and 3.3](#)) interaction. Compound D2 has a hydrogen bond interaction with Ala-213 where the amino group of Ala-213 donates a hydrogen to the nitrogen in position 9 of the imidazo[1,2-b]pyridazine backbone of D2. A T-shaped  $\pi$ - $\pi$  stacking interaction between D2 and Phe-144, where the positively charged framework of the D2 aromatic ring interacts with the  $\pi$  electron cloud of the aromatic ring of Phe-144. This seems to serve as a stabilizing interaction. In another stabilizing interaction, D2 acts as a hydrogen acceptor at the hydroxyl group of its benzyl alcohol sidechain accepting the hydrogen donated by the amino backbone of Thr-217. The final stabilizing interaction is the formation of a water bridge between Phe-275 (donor) and a water molecule (acceptor), the hydroxyl group of the phenyl group acts as donor for the water molecule and the water molecule acts as donor for Gln-185 and Glu-181. The strong stabilizing interactions of D2 with AURKA predicts good protein-ligand interaction *in-vivo*<sup>112-114</sup>.

As is the case with BRD4 and AURKA, there is a watershed interaction between AURKB and its inhibitors. AURKB, like AURKA has a hinge region that plays an important role in the binding of inhibitors to the ATP catalytic site. The conserved hinge residue in AURKB is Ala-173<sup>112,115</sup>. D2 interacts with Ala-173 as a hydrogen bond acceptor. The amino group of Ala-173 acts as hydrogen bond donor and nitrogen 9 of the imidazo[1,2-b]pyridazine backbone of D2. The rest of the interactions between AURKB and D2 are stabilizing interactions. A water bridge forms between D2, the hydrogen bond donor from the hydroxyl group of the phenol sidechain, the water molecule that acts as the acceptor for D2, as well as the hydrogen bond donated by the protonated lysyl side chain of Lys-122, and Asp-234 acts as the hydrogen bond acceptor from the water molecule. The hydroxyl group of the benzyl alcohol side chain of D2 donates a hydrogen bond to the carboxylic acid oxygen of Lys-101. These interactions seem to be indicators of success as inhibitors, Al-Sanea *et.al* previously reported on similar interactions in successful AURKB inhibitors *in silico*<sup>112</sup>.

Compound D2 forms a key hydrogen bond interaction with the Met-793 residue of the EGFR-TK. The Met-793 forms part of the hinge region of the protein, connecting the C- and N-lobe, hydrogen bonding with this residue is a known interaction displayed by

the two known EGFR-TK inhibitors, gefitinib and erlotinib<sup>117,123-124</sup>. The amino backbone of Met-793 donates a hydrogen bond to the nitrogen in spot nine of the imidazo[1,2-b]pyridazine backbone. This type of interaction, where the Met-793 backbone act as a hydrogen bond donor has previously been reported on<sup>117</sup>. Compound D2 has a hydrogen bond donor interaction between the hydroxyl group of the benzyl alcohol of D2 and the carbonic acid sidechain of Asp-855, and the hydrogen donor interaction between the protonated lysyl sidechain of Lys-745 (donor) and that same hydroxyl group of D2 (acceptor). This interaction with Asp-855 and Lys-745 seems like a conserved interaction, previously also reported in other studies<sup>117,123</sup>. The interaction with Asp-855 could be an indicator of inhibitor effectivity<sup>117</sup>. Asp-855 is part of the DFG motif (so named due to the amino acids it is made up of, namely Asp-855 or D-855, Phe-856 or F-856, and Gly-857 or G-857), when the DFG motif is in the “in” motif, the EGFR protein is in active conformation state, if the DFG motif is in the “out” motif, the EGFR protein is in an inactive state<sup>115,125</sup>. The “in” motif decreases the number of residues available for binding in the active site (only Asp-855 of the DFG), whereas the “out” conformation increases the availability of residues to bind (both Asp-855 and Phe-856 of the DFG can extend into the binding site)<sup>125</sup>. This means that D2 can possibly effectively bind EGFR, in both the active and inactive state (only Asp-855 interacts with the binding site, thus DFG is in the “out” motif)<sup>125</sup>. The  $\pi$ - $\pi$  stacking interaction between Phe-723 is a very interesting interaction because Phe-723, which forms a part of the P-loop, faces the inside of the active site decreasing the accessibility of the active site to its substrates and inhibitors<sup>117</sup>. Thus, what would usually decrease effectivity, might now be playing a role in stabilization of the inhibitor within the TK binding pocket. The  $\pi$ - $\pi$  stacking interaction is T-shaped, the positively charged framework of the Phe-723 aromatic ring interacts with the  $\pi$  electron cloud of the aromatic D2 phenol sidechain.

From the CV screening of compounds D2-D11 in MDA-MB-231 cells, it was possible to calculate a preliminary  $IC_{50}$  for D2 of 0.1739  $\mu$ M, this does not differ much from the  $IC_{50}$  calculated using the results of the MTT assay (0.1968  $\mu$ M), the gold standard in  $IC_{50}$  determination. The  $IC_{50}$  calculated from the MTT results is viewed as more reliable and was thus used in all further experiments<sup>126</sup>. The higher concentration from the MTT assay, can be ascribed to the fact that the MTT assay makes use of metabolic

activity as an indicator of viability, as opposed to the CV assay that bases viability solely on adherence to the wells<sup>126-127</sup>.

No significant difference between the OD of control and vehicle control of MDA-MB-231 was noted, thus all other experiments only made use of a vehicle control. Treatment of EA.hy926 cells caused no significant decreases in viability relative to the vehicle control. From this it is assumed that the IC<sub>50</sub> of D2 for the MDA-MB-231 cells is significantly lower than what the IC<sub>50</sub> for the EA.hy926 cells would be. The reason no IC<sub>50</sub> for the EA.hy926 cells were calculated is because the focus is on TNBC models, and whatever concentration is cytotoxic to them should be tested against a reference cell line in order for it to be possible to truly compare the effect D2 has on a TNBC cell line vs a somatic reference cell line.

The ELISA results ([Figure 3.16 and 3.17](#)) confirmed that there is definite expression of two of the targets, namely BRD4 and AURKA. Additionally, quantification of the concentrations of both BRD4 and AURKA after D2 treatment produced interesting results. The concentration of BRD4 in D2 treated MDA-MB-231 cells relative to the VC, was significantly decreased. This correlates with some other studies of BRD4 inhibitors where the inhibitor seems to cause a decrease in BRD4 expression<sup>128-130</sup>. The VC treatment of the EA.hy926 cells had a higher concentration of BRD4 compared to the MDA-MB-231 cells, and contrary to what was observed in the MDA-MB-231 cells, the D2-treated EA.hy926 cells had a significantly higher concentration of BRD4 compared to the VC, this has also been observed by other researchers<sup>131</sup>.

The AURKA ELISA results ([Figure 3.17](#)) indicated a significant decrease in AURKA concentration in the D2 treated MDA-MB-231 cells, relative to the VC. The concentration of AURKA in the VC-treated EA.hy926 cells were not different compared to the D2-treated cells.

Flow cytometric analysis of the cell cycle in D2-treated MDA-MB-231 cells ([Figure 3.20](#)), highlighted a decrease in the percentage of cells in S-phase, a result consistent with BRD4 inhibition as well as AURKB inhibition<sup>129,132-134</sup>. BRD4 plays multiple roles in the modulation of the cell cycle, especially entry of cells into the S-phase of the cell cycle by promoting the transcription of genes important in the progression from G1 to S<sup>132</sup>. BRD4 stimulates the binding of RNA Pol II and P-TEFb to the promoters of G1 genes, leading to transcriptional elongation and G1 progression<sup>133</sup>. AURKB has a

canonical role in the CPC, regulating mitotic progression by means of the spindle assembly checkpoint, preventing progression if there are aberrant microtubule-kinetochore attachments<sup>134</sup>. However, the results here, and those obtained by others suggest an additional role of AURKB, that of a modulator of G1-S progression<sup>134-136</sup>. AURKB can form a complex with mTOR and regulate specific epigenetic markers that play roles in the transition of G1 to S<sup>134-135</sup>. Additionally, AURKB has been shown to directly phosphorylate p53, leading to decreased expression of p53 target genes, and thus G1-S progression<sup>134,136</sup>. The D2-treated EA.hy926 cells ([Figure 3.21](#)) showed a significant increase of cells in the S-phase and a significant decrease of cells in the G2/M phase. These results do not correlate with BRD4 inhibition, something that might be ascribed to the increase in BRD4 in D2 treated cells ([Figure 3.16](#)), where increased expression of BRD4 might overcome its inhibition<sup>131</sup>. The increase in the number of cell in S-phase correlates with EGFR inhibition, however it is more common to see significant increases in G2/M cell numbers due to arrest in the mitotic phase. The effect of D2 on the cell cycle of the EA.hy926 cells does not correlate with that of the MDA-MB-231 results. This might be explained by the fact that D2 is a poly-inhibitor and could thus be having an effect on multiple downstream effectors of the targets proteins. For instance, research has shown that p21 and p27 expression is upregulated when BRD4 is inhibited and p27 is upregulated when AURKA, and AURKB are inhibited<sup>133,137-139</sup>. The upregulation of p21 and p27 then leads to inhibition of the cell cycle and could lead to cell cycle arrest, but only in G0/G1 and G2/M which does not explain the S-phase arrest<sup>133,138-139</sup>. A possible explanation for the S-phase arrest in the D2 treated cells is the accumulation of double stranded breaks due to ROS<sup>140-141</sup>. Increased ROS due to treatment with D2 could have led to an increase in double stranded breaks, which leads to activation of the checkpoint kinase 1 and 2, causing the cells to arrest in S-phase in order for the cellular machinery to repair the double stranded breaks<sup>140-141</sup>. A potential reason for the lack of S-phase arrest in the D2 treated MDA-MB-231 cells is the fact that they are cancerous in nature, as opposed to the EA.hy926 cells which serve as a model of transformed (hybridized) umbilical vein endothelial cells, and they might have mutated machinery for double stranded break repair<sup>142</sup>. Heterogeneity in cancer is a favourable trait for cellular survival and proliferation, a trait which is the result of genomic instability<sup>142</sup>. This genomic instability can be induced by the cancer cells via dysregulation (and not complete silencing) of the double stranded break repair pathways<sup>142</sup>. Normally increased time spent in the

cell-phase where the double stranded break was identified (S-phase arrest for instance) increases the chances of correct repair by for instance homologous recombination, which could be the case in the D2-treated EA.hy926 cells<sup>142</sup>. But in cancerous cells such as MDA-MB-231 cells, it is probable that the repair process favours a “quick fix” with lower fidelity, such as non-homologous end joining (NEHJ), above homologous recombination which has high fidelity to ensure genomic stability<sup>142</sup>.

D2-treatment of the MDA-MB-231 cells caused a significant increase in ROS relative to the VC (Figure 3.24). An increase in ROS in the D2-treated EA.hy926 cells (Figure 3.25) was also observed, however the increase was not as steep as seen in the D2-treated MDA-MB-231 cells. This is a result consistent with EGFR and AURKA inhibition according to literature<sup>143-145</sup>. ROS in physiological normal quantities play a role in EGFR activity, specifically H<sub>2</sub>O<sub>2</sub> which almost act as a second messenger molecule. EGFR phosphorylation is greatly enhanced by the presence of H<sub>2</sub>O<sub>2</sub> by means of oxidation of specific residues, which increases downstream signalling. The EGFR half-life seems to be additionally increased by exposure to H<sub>2</sub>O<sub>2</sub>, from 8 h when activated by EGF to about 18 h following H<sub>2</sub>O<sub>2</sub> activation<sup>146</sup>. However, here the levels of ROS in the D2-treated cells, significantly exceed the levels found in the VC. Normally when EGF and/or EGFR is (over) expressed in cancer cells they perform a protective function, by inhibiting ROS over production and resultant toxicity<sup>144</sup>. EGF actively blocks the ROS producing activity of transforming growth factor-beta (TGF-β)<sup>144</sup>. TGF-β normally functions as a tumour suppressor cytokine, by inducing cell cycle arrest and apoptosis<sup>144</sup>. However, cancer cells seem to acquire resistance to its signals, causing it to rather modulate invasion and metastasis<sup>144</sup>. It does this in part by producing anti-apoptotic ligands that bind to EGFR, activating it, and in so doing, it protects the cancer cells from ROS<sup>144</sup>. But once EGFR is inhibited, TGF-β can stimulate the production of ROS. It does so in two ways, by downregulating the genes of mitochondrial antioxidant genes, such as glutathione, and by activating NADPH-Oxidase<sup>144</sup>. This upregulation of ROS production re-sensitizes the cancer cells to TGF-β induced-apoptosis. The increase in ROS also correlates to the effects observed when AURKA is knocked down in oral squamous cell carcinoma (OSCC) which leads to increased ROS production, beyond the threshold that the cancer cells can weather<sup>145</sup>. In a study of AURKB inhibition it was observed that ROS production is

greatly upregulated causing downregulation of key molecules of differentiation and upregulating activated caspase 3<sup>147</sup>. Inhibition of BRD4, contrastingly, seems to lead to a decrease in ROS by means of upregulated expression of the cytoprotective heme oxygenase-1 (HMOX1)<sup>148</sup>.

Analysis of the apoptotic profiles of the D2-treated MDA-MB-231 cells ([Figure 3.28](#)), showed a significant increase in apoptosis relative to the VC. This correlates with marked increase in ROS, which could be due to the inhibition of EGFR and subsequent induction of TFG- $\beta$  mediated-apoptosis<sup>144</sup>. BRD4 inhibition has been shown to induce apoptosis in more than one way<sup>149-150</sup>. It can lead to the suppression of NF- $\kappa$ B activation causing the activation of tumour necrosis factor-related apoptosis-inducing ligand (TRAIL) which binds to the death receptors-4 and -5, to form a trimer that recruits the Fas-associated death domain (FADD), that in turn recruits, activates and binds to caspase-8, triggering the induction of apoptosis<sup>149</sup>. In another study BRD4 inhibition led to decreased levels of the anti-apoptotic B-cell lymphoma-2 (Bcl-2) protein and increased levels of Bcl-2-associated X (BAX) protein and activated caspase 3<sup>150</sup>. BAX, because it is no longer inhibited by the anti-apoptotic Bcl-2, can translocate to the mitochondria where it oligomerizes with Bcl-2 homologous antagonist killer (BAK) forming pores, liberating cytochrome C<sup>150</sup>. Cytochrome C activates the apoptotic protease activating factor-1 (Apaf-1) which eventually leads to the activation of caspase-3, committing the cell to apoptosis<sup>150</sup>. Studies have shown that AURKA inhibition leads to increased ROS production as well as an increased expression of poly (ADP)-ribose polymerase (PARP) and an increase in activated caspase 3 leading to increased apoptotic events<sup>145</sup>. Increased PARP leads to an increase in caspase-independent apoptosis<sup>145</sup>. Inhibiting AURKB has been shown to increase the number of activated caspase 3, leading to increased apoptosis<sup>147</sup>. The D2-treated EA.hy926 cells ([Figure 3.29](#)) showed no significant difference in the number of apoptotic cells, consistent with the relatively small increase in ROS. It did however show a small but significant increase in the amount of dead or necrotic cells relative to the VC, which could be due to the upregulation in BRD4 concentration observed from the ELISA, which means ROS is increased but pro-apoptotic molecules such as caspase 3, and BAX is inhibited, leading to necrotic cell death instead of apoptotic cell death<sup>151</sup>.

## 5. Conclusion

In conclusion, *in silico* HTVS of the Biofocus library of 20 000 compounds, firstly in BRD4, consequently yielding 79 hits with docking scores  $\leq -9$ . These 79 compounds were then docked into AURKA, AURKB, PLK1, and EGFR. This produced only ten compounds with docking scores  $\leq -9$  for the different kinases. Screening of the compounds *in vitro* using CV proved successful for only one compound, D2. From the HTVS results, D2 was assumed to be a poly-inhibitor of BRD4 via BD1, EGFR via the TK binding pocket, and AURKA and AURKB via the ATP catalytic site.

The  $IC_{50}$  of D2 was determined after 48 h of treatment, as 0.1968  $\mu\text{M}$  using the MTT cytotoxicity assay in MDA-MB-231. Consequent treatment of EA.hy926 with the MDA-MB-231 determined  $IC_{50}$  of D2 had no significant effect on viability based on MTT results. Compound D2 is thus a potential poly-inhibitor with nanomolar potency.

Elucidation of presence of two of the targets, BRD4 and AURKA, proved positive, with both MDA-MB-231 and EA.hy926 cells having sufficiently high concentrations of the two target protein. Cell cycle analysis of D2-treated MDA-MB-231 cells had results consistent with BRD4 and AURKB inhibition, namely decreased cells in S-phase. And the analysis of EA.hy926 cells had results consistent with ROS induced double stranded breaks and S-phase arrest. The significant increases in ROS in MDA-MB-231 cells and to a lesser extent in the EA.hy926 cells, following treatment with the D2  $IC_{50}$  was consistent with the assumption that D2 inhibits AURKA, AURKB, and EGFR. This significant upregulation of ROS production together with the assumed expression, activation and modulation of pro-apoptotic molecules in response to BRD4, AURKA, AURKB, and EGFR inhibition led to a very significant increase in apoptosis in the MDA-MB-231 cells and to necrosis in the EA.hy926 cells.

Taking all of the results into account, it is assumed that D2 is in fact a poly-inhibitor of BRD4, AURKA, AURKB, and EGFR. This is a novel therapeutic approach to target these four specific proteins. Targeting multiple proteins of interest could potentially mean higher therapeutic outcomes coupled with decreased resistance. For instance dual BRD4 and AURKA inhibition prevents resistance to AURKA treatment alone<sup>53</sup>. However these results do not prove this assumption in its entirety, it is necessary to

further investigate the mechanistic effect of D2. Expression profiles need to be tested, especially with regards to c-Myc. Additionally enzyme kinetics in the presence of D2 need to be tested. Additionally, to validate the HTVS results, X-ray crystallography of D2 bound to its target proteins could prove useful.

## 6. References

1. Huang J, Chan PS, Lok V, Chen X, Ding H, Jin Y, et al. Global incidence and mortality of breast cancer: A trend analysis. *Aging*. 2021; 13(4):5748-803.
2. Lei S, Zheng R, Zhang S, Wang S, Chen R, Sun K, et al. Global patterns of breast cancer incidence and mortality: A population-based cancer registry data analysis from 2000 to 2020. *Cancer communications (London, England)*. 2021; 41(11):1183-94.
3. Deus CM, Serafim TL, Magalhaes-Novais S, Vilaca A, Moreira AC, Sardao VA, et al. Sirtuin 1-dependent resveratrol cytotoxicity and pro-differentiation activity on breast cancer cells. *Arch Toxicol*. 2017; 91(3):1261-78.
4. Hanahan D, Weinberg RA. Hallmarks of cancer: The next generation. *Cell*. 2011; 144(5):646-74.
5. Senga S. Hallmarks of cancer. *Eur J Cancer Prev*. 2021; 31(Supplement 1):S11.
6. Dawood SD. Triple-negative breast cancer : Epidemiology and management options. *Drugs*. 2010; 70(17):2247-58.
7. Moreira MP, Brayner FbA, Alves LC, Cassali GD, Silva LM. Phenotypic, structural, and ultrastructural analysis of triple-negative breast cancer cell lines and breast cancer stem cell subpopulation. *European Biophysics Journal : with Biophysics Letters*. 2019; 48(7):673-84.
8. Willems E, Lombard A, Dedobbeleer M, Goffart N, Rogister B. The unexpected roles of aurora a kinase in glioblastoma recurrences. *Target Oncol*. 2017; 12(1):11-8.
9. Chhabra SN, Booth BW. Asymmetric cell division of mammary stem cells. *Cell Div*. 2021; 16(1):5.
10. Sugiarto S, Persson AI, Munoz EG, Waldhuber M, Lamagna C, Andor N, et al. Asymmetry-defective oligodendrocyte progenitors are glioma precursors. *Cancer Cell*. 2011; 20(3):328-40.
11. Wu M, Kwon HY, Rattis F, Blum J, Zhao C, Ashkenazi R, et al. Imaging hematopoietic precursor division in real time. *Cell Stem Cell*. 2007; 1(5):541-54.
12. Micalizzi DS, Farabaugh SM, Ford HL. Epithelial-mesenchymal transition in cancer: Parallels between normal development and tumor progression. *J Mammary Gland Biol Neoplasia*. 2010; 15(2):117-34.
13. Cortesi M, Liverani C, Mercatali L, Ibrahim T, Giordano E. Computational models to explore the complexity of the epithelial to mesenchymal transition in cancer. *Wiley interdisciplinary reviews. Systems biology and medicine*. 2020; 12(6):e1488.
14. Morel AP, Lièvre M, Thomas C, Hinkal G, Ansieau S, Puisieux A. Generation of breast cancer stem cells through epithelial-mesenchymal transition. *PLoS One*. 2008; 3(8):e2888.
15. Hapke RY, Haake SM. Hypoxia-induced epithelial to mesenchymal transition in cancer. *Cancer Lett*. 2020; 487:10-20.
16. Williams GH, Stoeber K. The cell cycle and cancer. *The Journal of Pathology*. 2012; 226(2):352-64.
17. Johnson DG, Walker CL. Cyclins and cell cycle checkpoints. *Annu Rev Pharmacol Toxicol*. 1999; 39:295-312.
18. Bartek J, Bartkova J, Lukas J. The retinoblastoma protein pathway and the restriction point. *Curr Opin Cell Biol*. 1996; 8(6):805-14.
19. Damodaran AP, Vaufrey L, Gavard O, Prigent C. Aurora a kinase is a priority pharmaceutical target for the treatment of cancers. *Trends Pharmacol Sci*. 2017; 38(8):687-700.
20. Day PJ, Cleasby A, Tickle IJ, O'Reilly M, Coyle JE, Holding FP, et al. Crystal structure of human cdk4 in complex with a d-type cyclin. *Proc Natl Acad Sci U S A*. 2009; 106(11):4166-70.
21. Hamilton E, Infante JR. Targeting cdk4/6 in patients with cancer. *Cancer Treat Rev*. 2016; 45:129-38.
22. Murphy CG, Dickler MN. The role of cdk4/6 inhibition in breast cancer. *The Oncologist*. 2015; 20(5):483-90.

23. Dai M, Zhang C, Ali A, Hong X, Tian J, Lo C, et al. Cdk4 regulates cancer stemness and is a novel therapeutic target for triple-negative breast cancer. *Sci Rep.* 2016; 6(1).
24. Patel JM, Goss A, Garber JE, Torous V, Richardson ET, Haviland MJ, et al. Retinoblastoma protein expression and its predictors in triple-negative breast cancer. *npj Breast Cancer.* 2020; 6(1).
25. Tarrado-Castellarnau M, de Atauri P, Tarragó-Celada J, Perarnau J, Yuneva M, Thomson TM, et al. De novo myc addiction as an adaptive response of cancer cells to cdk4/6 inhibition. *Mol Syst Biol.* 2017; 13(10):940.
26. Liao S, Maertens O, Cichowski K, Elledge SJ. Genetic modifiers of the brd4-nut dependency of nut midline carcinoma uncovers a synergism between betis and cdk4/6is. *Genes Dev.* 2018; 32(17-18):1188-200.
27. Zhao Y, Liu Q, Acharya P, Stengel Kristy R, Sheng Q, Zhou X, et al. High-resolution mapping of rna polymerases identifies mechanisms of sensitivity and resistance to bet inhibitors in t(8;21) aml. *Cell Reports.* 2016; 16(7):2003-16.
28. Chapuy B, McKeown MR, Lin CY, Monti S, Roemer MG, Qi J, et al. Discovery and characterization of super-enhancer-associated dependencies in diffuse large b cell lymphoma. *Cancer Cell.* 2013; 24(6):777-90.
29. Donati B, Lorenzini E, Ciarrocchi A. Brd4 and cancer: Going beyond transcriptional regulation. *Mol Cancer.* 2018; 17(1):164.
30. Ramadoss M, Mahadevan V. Targeting the cancer epigenome: Synergistic therapy with bromodomain inhibitors. *Drug discovery today.* 2018; 23(1):76-89.
31. Devaiah BN, Mu J, Akman B, Uppal S, Weissman JD, Cheng D, et al. Myc protein stability is negatively regulated by brd4. *Proc Natl Acad Sci U S A.* 2020; 117(24):13457-67.
32. Rahman S, Sowa ME, Ottinger M, Smith JA, Shi Y, Harper JW, et al. The brd4 extraterminal domain confers transcription activation independent of ptefb by recruiting multiple proteins, including nsd3. *Molecular and cellular biology.* 2011; 31(13):2641-52.
33. Zhang S, Roeder RG. The long and the short of brd4: Two tales in breast cancer. *Mol Cell.* 2020; 78(6):993-5.
34. Dey A, Chitsaz F, Abbasi A, Misteli T, Ozato K. The double bromodomain protein brd4 binds to acetylated chromatin during interphase and mitosis. *Proc Natl Acad Sci U S A.* 2003; 100(15):8758-63.
35. Devaiah BN, Gegonne A, Singer DS. Bromodomain 4: A cellular swiss army knife. *J Leukoc Biol.* 2016; 100(4):679-86.
36. Larue RC, Plumb MR, Crowe BL, Shkriabai N, Sharma A, DiFiore J, et al. Bimodal high-affinity association of brd4 with murine leukemia virus integrase and mononucleosomes. *Nucleic Acids Res.* 2014; 42(8):4868-81.
37. Devaiah BN, Lewis BA, Cherman N, Hewitt MC, Albrecht BK, Robey PG, et al. Brd4 is an atypical kinase that phosphorylates serine2 of the rna polymerase ii carboxy-terminal domain. *Proceedings of the National Academy of Sciences.* 2012; 109(18):6927-32.
38. Devaiah BN, Case-Borden C, Gegonne A, Hsu CH, Chen Q, Meerzaman D, et al. Brd4 is a histone acetyltransferase that evicts nucleosomes from chromatin. *Nature Structural & Molecular Biology.* 2016; 23:540.
39. Eilers M, Eisenman RN. Myc's broad reach. *Genes Dev.* 2008; 22(20):2755-66.
40. Zhang Y, Xu B, Shi J, Li J, Lu X, Xu L, et al. Brd4 modulates vulnerability of triple-negative breast cancer to targeting of integrin-dependent signaling pathways. *Cellular Oncology : The official journal of the International Society for Cellular Oncology* 2020. p. 1049-66.
41. Sankari N, Tareq H, Malik A, Zeynab N, Daniela I, Upasana B, et al. Bromodomain protein brd4 is required for estrogen receptor-dependent enhancer activation and gene transcription. *cell reports* 2014. p. 460-9.
42. Shu S, Lin CY, He HH, Witwicki RM, Tabassum DP, Roberts JM, et al. Response and resistance to bet bromodomain inhibitors in triple-negative breast cancer. *Nature.* 2016; 529(7586):413-7.
43. Lu L, Chen Z, Lin X, Tian L, Su Q, An P, et al. Inhibition of brd4 suppresses the malignancy of breast cancer cells via regulation of snail. *Cell Death Differ.* 2020; 27(1):255-68.

44. Qi L, Zhang Y. Alisertib (mln8237), a selective aurora-a kinase inhibitor, induces apoptosis in human tongue squamous cell carcinoma cell both in vitro and in vivo. *Tumor Biology : Tumor Markers, Tumor Targeting and Translational Cancer Research*. 2015; 36(3):1797-802.
45. Korobeynikov V, Borakove M, Feng Y, Wuest WM, Koval AB, Nikonova AS, et al. Combined inhibition of aurora a and p21-activated kinase 1 as a new treatment strategy in breast cancer. *Breast Cancer Res Treat*. 2019; 177(2):369-82.
46. Jalalirad M, Haddad TC, Salisbury JL, Radisky D, Zhang M, Schroeder M, et al. Aurora-a kinase oncogenic signaling mediates  $\text{tgf-}\beta$ -induced triple-negative breast cancer plasticity and chemoresistance. *Oncogene*. 2021; 40(14):2509-23.
47. Baldini E, D'Armiento M, Ulisse S. A new aurora in anaplastic thyroid cancer therapy. *Int J Endocrinol*. 2014; 2014:816430.
48. Colon NC, Schlegel CE, Qiao J, Chung DHVUMCNTN. Aurora a kinase regulates n-myc activity through phosphorylation of gsk3-beta and beta-catenin. *Journal of the American College of Surgeons: Supplement*. 2011; 213(3 Supplement):S82-S3.
49. Wang LH, Xiang J, Yan M, Zhang Y, Zhao Y, Yue CF, et al. The mitotic kinase aurora-a induces mammary cell migration and breast cancer metastasis by activating the cofilin-f-actin pathway. *Cancer Res*. 2010; 70(22):9118-28.
50. Yang S, He S, Zhou X, Liu M, Zhu H, Wang Y, et al. Suppression of aurora-a oncogenic potential by c-myc downregulation. *Exp Mol Med*. 2010; 42(11):759-67.
51. den Hollander J, Rimpì S, Doherty JR, Rudelius M, Buck A, Hoellein A, et al. Aurora kinases a and b are up-regulated by myc and are essential for maintenance of the malignant state. *Blood*. 2010; 116(9):1498-505.
52. Tentler JJ, Ionkina AA, Tan AC, Newton TP, Pitts TM, Glogowska MJ, et al. P53 family members regulate phenotypic response to aurora kinase a inhibition in triple-negative breast cancer. *Mol Cancer Ther*. 2015; 14(5):1117-29.
53. Felgenhauer J, Tomino L, Selich-Anderson J, Bopp E, Shah N. Dual brd4 and aurka inhibition is synergistic against mycn-amplified and nonamplified neuroblastoma. *Neoplasia (New York, N.Y.)*. 2018; 20(10):965-74.
54. You J, Li Q, Wu C, Kim J, Ottinger M, Howley PM. Regulation of aurora b expression by the bromodomain protein brd4. *Mol Cell Biol*. 2009; 29(18):5094-103.
55. Kwiatkowski N, Deng X, Wang J, Tan L, Villa F, Santaguida S, et al. Selective aurora kinase inhibitors identified using a taxol-induced checkpoint sensitivity screen. *ACS Chem Biol*. 2012; 7(1):185-96.
56. Yang D, Liu H, Goga A, Kim S, Yuneva M, Bishop JM. Therapeutic potential of a synthetic lethal interaction between the myc proto-oncogene and inhibition of aurora-b kinase. *Proc Natl Acad Sci U S A*. 2010; 107(31):13836-41.
57. Liao Y, Li J, Fan Y, Xu B. Polymorphisms in aurka and aurkb are associated with the survival of triple-negative breast cancer patients treated with taxane-based adjuvant chemotherapy. *Cancer Manag Res*. 2018; 10:3801-8.
58. Li J, Wang R, Schweickert PG, Karki A, Yang Y, Kong Y, et al. Plk1 inhibition enhances the efficacy of gemcitabine in human pancreatic cancer. *Cell Cycle*. 2016; 15(5):711-9.
59. Zhixian L, Qingrong S, Xiaosheng W. Plk1, a potential target for cancer therapy. *Transl Oncol* 2017. p. 22-32.
60. Mao F, Li J, Luo Q, Wang R, Kong Y, Carlock C, et al. Plk1 inhibition enhances the efficacy of bet epigenetic reader blockade in castration-resistant prostate cancer. *Mol Cancer Ther*. 2018; 17(7):1554-65.
61. Witkiewicz AK, Chung S, Brough R, Vail P, Franco J, Lord CJ, et al. Targeting the vulnerability of rb tumor suppressor loss in triple-negative breast cancer. *Cell reports*. 2018; 22(5):1185-99.
62. Sigismund S, Avanzato D, Lanzetti L. Emerging functions of the egfr in cancer. *Mol Oncol*. 2018; 12(1):3-20.

63. Ferguson KM. Structure-based view of epidermal growth factor receptor regulation. *Annual review of biophysics*. 2008; 37:353-73.
64. Sun XQ, Chen L, Li YZ, Li WH, Liu GX, Tu YQ, et al. Structure-based ensemble-qsar model: A novel approach to the study of the egfr tyrosine kinase and its inhibitors. *Acta Pharmacol Sin*. 2014; 35(2):301-10.
65. Iosifidou R, Galaktidou G, Albanaki XR, Mameletzi S, Vladika N, Patakiouta F, et al. Serum egfr and serum her2 in patients with triple negative breast cancer. *EJC Supplements*. 2008; 6(9):103-.
66. Liao W-S, Ho Y, Lin Y-W, Naveen Raj E, Liu K-K, Chen C, et al. Targeting egfr of triple-negative breast cancer enhances the therapeutic efficacy of paclitaxel- and cetuximab-conjugated nanodiamond nanocomposite. *Acta Biomaterialia*. 2019; 86:395-405.
67. Liu X, Li Q, Huang P, Tong D, Wu H, Zhang F. Egfr-mediated signaling pathway influences the sensitivity of oral squamous cell carcinoma to jq1. *J Cell Biochem*. 2018; 119(10):8368-77.
68. Moya-García A, Adeyelu T, Kruger FA, Dawson NL, Lees JG, Overington JP, et al. Structural and functional view of polypharmacology. *Sci Rep*. 2017; 7(1).
69. Antolin A, Workman P, Mestres J, Al-Lazikani B. Polypharmacology in precision oncology: Current applications and future prospects. *Curr Pharm Des*. 2017; 22(46):6935-45.
70. Clyde A, Galanie S, Kneller DW, Ma H, Babuji Y, Blaiszik B, et al. High-throughput virtual screening and validation of a sars-cov-2 main protease noncovalent inhibitor. *J Chem Inf Model*. 2021; 62(1).
71. Graff DE, Shakhnovich EI, Coley CW. Accelerating high-throughput virtual screening through molecular pool-based active learning. *Chem Sci*. 2021; 12(22):7866-81.
72. Kwon S, Bae H, Jo J, Yoon S. Comprehensive ensemble in qsar prediction for drug discovery. *BMC Bioinformatics* 2019.
73. Hert J, Willett P, Wilton DJ, Acklin P, Azzaoui K, Jacoby E, et al. New methods for ligand-based virtual screening: Use of data fusion and machine learning to enhance the effectiveness of similarity searching. *J Chem Inf Model*. 2006; 46(2):462-70.
74. Wang Z, Sun H, Shen C, Hu X, Gao J, Li D, et al. Combined strategies in structure-based virtual screening. *Phys Chem Chem Phys*. 2020; 22(6):3149-59.
75. Zhou Y, Jiang Y, Chen S-J. Rna-ligand molecular docking: Advances and challenges. *Wiley Interdisciplinary Reviews: Computational Molecular Science*. 2022; 12(3).
76. Batool M, Ahmad B, Choi S. A structure-based drug discovery paradigm. *Int J Mol Sci*. 2019; 20(11).
77. Friesner RA, Banks JL, Murphy RB, Halgren TA, Klicic JJ, Mainz DT, et al. Glide: A new approach for rapid, accurate docking and scoring. 1. Method and assessment of docking accuracy. *J Med Chem*. 2004; 47(Part 7):1739-49.
78. Guedes IA, de Magalhães CS, Dardenne LE. Receptor-ligand molecular docking. *Biophys Rev*. 2014; 6(1):75-87.
79. Madhavi Sastry G, Adzhigirey M, Day T, Annabhimoju R, Sherman W. Protein and ligand preparation: Parameters, protocols, and influence on virtual screening enrichments. *Journal of Computer-Aided Molecular Design : Incorporating Perspectives in Drug Discovery and Design*. 2013; 27(3):221-34.
80. Corbeil CR, Moitessier N. Docking ligands into flexible and solvated macromolecules. 3. Impact of input ligand conformation, protein flexibility, and water molecules on the accuracy of docking programs. *J Chem Inf Model*. 2009; 49(4):997-1009.
81. Allen BK, Mehta S, Schurer SC, Ayad NG, Ember SWJ, Zhu JY, et al. Identification of a novel class of brd4 inhibitors by computational screening and binding simulations. *ACS Omega*. 2017; 2(8):4760-71.
82. Mysinger MM, Carchia M, Irwin JJ, Shoichet BK. Directory of useful decoys, enhanced (dud-e): Better ligands and decoys for better benchmarking. *J Med Chem*. 2012; 55(14):6582-94.
83. Cleves AE, Jain AN. Structure- and ligand-based virtual screening on dud-e+: Performance dependence on approximations to the binding pocket. *J Chem Inf Model*. 2020; 60(9):4296-310.

84. Hosmer DW, Lemeshow S, Sturdivant RX. Applied logistic regression. 3rd ed. ed. Chichester: Wiley; 2013.
85. Craig IR, Essex JW, Spiegel K. Ensemble docking into multiple crystallographically derived protein structures: An evaluation based on the statistical analysis of enrichments. *J Chem Inf Model*. 2010; 50(4):511-24.
86. Elokely KM, Doerksen RJ. Docking challenge: Protein sampling and molecular docking performance. *J Chem Inf Model*. 2013; 53(8):1934-45.
87. Greenwood JR, Calkins D, Sullivan AP, Shelley JC. Towards the comprehensive, rapid, and accurate prediction of the favorable tautomeric states of drug-like molecules in aqueous solution. *Journal of Computer-Aided Molecular Design : Incorporating Perspectives in Drug Discovery and Design*. 2010; 24(6-7):591-604.
88. Wagner K-U. Know thy cells: Commonly used triple-negative human breast cancer cell lines carry mutations in ras and effectors. *Breast cancer research : BCR*. 2022; 24(1):44.
89. Małgorzata G, Karol K, Bartłomiej G, Stefania P, Marie Angele C, Martina D, et al. Novel tetrahydroacridine derivatives with iodobenzoic moieties induce g0/g1 cell cycle arrest and apoptosis in a549 non-small lung cancer and ht-29 colorectal cancer cells. *Mol Cell Biochem* 2019. p. 1-28.
90. Feoktistova M, Geserick P, Leverkus M. Crystal violet assay for determining viability of cultured cells. *Cold Spring Harb Protoc*. 2016; 2016(4):pdb.prot087379.
91. Enciso-Benavides J, Alfaro L, Castañeda-Altamirano C, Rojas N, González-Cabeza J, Enciso N, et al. Biological characteristics of a sub-population of cancer stem cells from two triple-negative breast tumour cell lines. *Heliyon*. 2021; 7(6):e07273.
92. Samson J, Derlipanska M, Zaheed O, Dean K. Molecular and cellular characterization of two patient-derived ductal carcinoma in situ (dcis) cell lines, etcc-006 and etcc-010. *BMC Cancer*. 2021; 21(1):790.
93. Damiani E, Solorio JA, Doyle AP, Wallace HM. How reliable are in vitro ic50 values? Values vary with cytotoxicity assays in human glioblastoma cells. *Toxicol Lett*. 2019; 302:28-34.
94. Dubois C, Martin F, Hassel C, Magnier F, Daumar P, Aubel C, et al. Low-dose and long-term olaparib treatment sensitizes mda-mb-231 and sum1315 triple-negative breast cancers spheroids to fractionated radiotherapy. *Journal of Clinical Medicine*. 2020; 9(1):64.
95. Kahl I, Mense J, Finke C, Boller A-L, Lorber C, Györfy B, et al. The cell cycle-related genes rhamm, aurka, tpx2, plk1, and plk4 are associated with the poor prognosis of breast cancer patients. *J Cell Biochem*. 2022; 123(3):581-600.
96. Yang G-J, Song Y-Q, Wang W, Han Q-B, Ma D-L, Leung C-H. An optimized brd4 inhibitor effectively eliminates nf-kb-driven triple-negative breast cancer cells. *Bioorg Chem*. 2021; 114:105158.
97. Thandi Mqoco tmuaaz, André Stander asuaz, Anna-Mart Engelbrecht asaz, Anna MJajuaz. A combination of an antimetabolic and a bromodomain 4 inhibitor synergistically inhibits the metastatic mda-mb-231 breast cancer cell line. *BioMed Research International*. 2019; 2019.
98. Alhaji M, Farhana A. Enzyme linked immunosorbent assay. Statpearls. Treasure Island (FL): StatPearls Publishing
- Copyright © 2022, StatPearls Publishing LLC.; 2022.
99. Christine V, Christelle D, Marie-Thérèse G, Didier B, Emmanuel G, Philippe R, et al. Flow cytometric quantification of all phases of the cell cycle and apoptosis in a two-color fluorescence plot. *PLoS One* 2013.
100. Kuksin D, Kuksin CA, Qiu J, Chan LL-Y. Cellometer image cytometry as a complementary tool to flow cytometry for verifying gated cell populations. *Anal Biochem*. 2016; 503:1-7.
101. Davies D. Flow cytometric analysis of cell cycle with propidium iodide DNA staining. *ABCAM* 2018.
102. Perillo B, Di Donato M, Pezone A, Di Zazzo E, Giovannelli P, Galasso G, et al. Ros in cancer therapy: The bright side of the moon. *Exp Mol Med*. 2020; 52(2):192-203.
103. Cheung EC, Vousden KH. The role of ros in tumour development and progression. *Nature Reviews Cancer*. 2022; 22(5):280-97.

104. Rao S, Sanschagrin PC, Greenwood JR, Repasky MP, Sherman W, Farid R. Improving database enrichment through ensemble docking. *Journal of Computer-Aided Molecular Design : Incorporating Perspectives in Drug Discovery and Design*. 2008; 22(9):621-7.
105. Abelian A, Dybek M, Wallach J, Gaye B, Adejare A. Chapter 6 - pharmaceutical chemistry. In: Adejare A, editor. *Remington (twenty-third edition)*: Academic Press; 2021. p. 105-28.
106. Frey PA. Low-barrier hydrogen bonds. In: Lennarz WJ, Lane MD, editors. *Encyclopedia of biological chemistry (second edition)*. Waltham: Academic Press; 2013. p. 756-9.
107. Zhuang W-R, Wang Y, Cui P-F, Xing L, Lee J, Kim D, et al. Applications of  $\pi$ - $\pi$  stacking interactions in the design of drug-delivery systems. *J Control Release*. 2019; 294:311-26.
108. Mahadevi AS, Sastry GN. Cation- $\pi$  interaction: Its role and relevance in chemistry, biology, and material science. *Chem Rev*. 2013; 113(3):2100-38.
109. Jung M, Philpott M, Müller S, Schulze J, Badock V, Eberspächer U, et al. Affinity map of bromodomain protein 4 (brd4) interactions with the histone h4 tail and the small molecule inhibitor jq1\*. *The Journal of Biological Chemistry*. 2014; 289(13):9304-19.
110. Bamborough P, Chung C-w. Fragments in bromodomain drug discovery. *MedChemComm*. 2015; 6(9):1587-604.
111. Zhiqing L, Pingyuan W, Haiying C, Wold EA, Bing T, Brasier AR, et al. Drug discovery targeting bromodomain-containing protein 4. *J Med Chem*. 2017; 60(11).
112. Al-Sanea MM, Elkamhawy A, Paik S, Lee K, El Kerdawy AM, Syed Nasir Abbas B, et al. Sulfonamide-based 4-anilinoquinoline derivatives as novel dual aurora kinase (aurka/b) inhibitors: Synthesis, biological evaluation and in silico insights. *Bioorg Med Chem*. 2020; 28(13).
113. Chinnasamy S, Selvaraj G, Kaushik AC, Kaliampurthi S, Chandrabose S, Singh SK, et al. Molecular docking and molecular dynamics simulation studies to identify potent aurka inhibitors: Assessing the performance of density functional theory, mm-gbsa and mass action kinetics calculations. *J Biomol Struct Dyn*. 2020; 38(14):4325-35.
114. Kim J-T, Jung SH, Kang SY, Ryu C-K, Kang NS, Christov CZ. The discovery of aurora kinase inhibitor by multi-docking-based virtual screening. *Int J Mol Sci*. 2014; 15(11):20403-12.
115. Ghose AK, Herbertz T, Pippin DA, Salvino JM, Mallamo JP. Knowledge based prediction of ligand binding modes and rational inhibitor design for kinase drug discovery. *J Med Chem*. 2008; 51(17):5149-71.
116. Li DD, Wu TT, Yu P, Zhao LG, Jiang Y, Wang ZZ, et al. Molecular dynamics analysis of binding sites of epidermal growth factor receptor kinase inhibitors. *ACS Omega*. 2020; 5(26):16307-14.
117. Yoshikawa S, Kukimoto-Niino M, Parker L, Handa N, Terada T, Fujimoto T, et al. Structural basis for the altered drug sensitivities of non-small cell lung cancer-associated mutants of human epidermal growth factor receptor. *Oncogene*. 2012; 32(1):27-38.
118. Carlson HA. Check your confidence: Size really does matter. *J Chem Inf Model*. 2013; 53(8):1837-41.
119. Theodoulou NH, Bamborough P, Bannister AJ, Becher I, Bit RA, Ka Hing C, et al. Discovery of i-brd9, a selective cell active chemical probe for bromodomain containing protein 9 inhibition. *J Med Chem*. 2016; 59(4).
120. Vollmuth F, Blankenfeldt W, Geyer M. Structures of the dual bromodomains of the p-tefb-activating protein brd4 at atomic resolution. *J Biol Chem*. 2009; 284(52):36547-56.
121. Kuang M, Wang L, Guo J, Zhou J, Liu Z, Wu R. Binding kinetics versus affinities in brd4 inhibition. *J Chem Inf Model*. 2015; 55(9):1926-35.
122. Wang Y, Wu S, Wang L, Zhao J, Zhang L, Yang Z. Binding selectivity of inhibitors toward the first over the second bromodomain of brd4: Theoretical insights from free energy calculations and multiple short molecular dynamics simulations. *RSC Advances*. 2020; 11(2):745-59.
123. Sharma V, Nandekar P, Sangamwar A, Perez-Sanchez H, Agarwal S. Structure guided design and binding analysis of egfr inhibiting analogues of erlotinib and aee788 using ensemble docking, molecular dynamics and mm-gbsa. *RSC ADVANCES*. 2016; 6(70):65725-35.

124. Yun CH, Boggon TJ, Li Y, Woo MS, Greulich H, Meyerson M, et al. Structures of lung cancer-derived egfr mutants and inhibitor complexes: Mechanism of activation and insights into differential inhibitor sensitivity. *Cancer Cell*. 2007; 11(3):217-27.
125. Peng Y-H, Shiao H-Y, Tu C-H, Liu P-M, Hsu JT-A, Amancha PK, et al. Protein kinase inhibitor design by targeting the asp-phe-gly (dfg) motif: The role of the dfg motif in the design of epidermal growth factor receptor inhibitors. *J Med Chem*. 2013; 56(10):3889-903.
126. Mangis J, Mansur TB, Kern KM, Schroeder JR. Selection of an optimal cytotoxicity assay for undergraduate research. *Bioscene: The Journal Of College Biology Teaching*. 2019; 45:24-32.
127. Edwards V, Markovic E, Matisons J, Young F. Development of an in vitro reproductive screening assay for novel pharmaceutical compounds. *Biotechnol Appl Biochem*. 2008; 51(2):63-71.
128. Liu S, Li F, Pan L, Yang Z, Shu Y, Lv W, et al. Brd4 inhibitor and histone deacetylase inhibitor synergistically inhibit the proliferation of gallbladder cancer in vitro and in vivo. *Cancer Sci*. 2019; 110(8):2493-506.
129. Coudé MM, Braun T, Berrou J, Dupont M, Bertrand S, Masse A, et al. Bet inhibitor otx015 targets brd2 and brd4 and decreases c-myc in acute leukemia cells. *Oncotarget*. 2015; 6(19):17698-712.
130. Li Y, Lin J, Wu Y, Wang X, Xiang J, Zhang J. Inhibition of brd4 by jq1 promotes functional recovery from spinal cord injury by activating autophagy. *Front Cell Neurosci*. 2020; 14.
131. Lu J, Qian Y, Altieri M, Dong H, Wang J, Raina K, et al. Hijacking the e3 ubiquitin ligase cereblon to efficiently target brd4. *Chem Biol*. 2015; 22(6):755-63.
132. Lam FC, Huang Q, Maffa AD, Kasper EM, Yaffe MB. Brd4 prevents the accumulation of r-loops and protects against transcription–replication collision events and DNA damage. *Nature Communications*. 2020; 11(1).
133. Zhang Y, Duan S, Jang A, Mao L, Liu X, Huang G. Jq1, a selective inhibitor of brd4, suppresses retinoblastoma cell growth by inducing cell cycle arrest and apoptosis. *Exp Eye Res*. 2021; 202.
134. Trakala M, Fernandez-Miranda G, De Castro IP, Malumbres M, Heeschen C. Aurora b prevents delayed DNA replication and premature mitotic exit by repressing p21<sup>sup</sup><sup>cip1</sup>. *Cell Cycle*. 2013; 12(7):1030-41.
135. Song J, Salek-Ardakani S, So T, Croft M. The kinases aurora b and mtor regulate the g1-s cell cycle progression of t lymphocytes. *Nat Immunol*. 2007; 8(1):64-73.
136. Wu L, Ma CA, Zhao Y, Jain A. Aurora b interacts with nir-p53, leading to p53 phosphorylation in its DNA-binding domain and subsequent functional suppression. *J Biol Chem*. 2011; 286(3):2236-44.
137. Görgün G, Calabrese E, Hideshima T, Ecsedy J, Perrone G, Mani M, et al. A novel aurora-a kinase inhibitor mln8237 induces cytotoxicity and cell-cycle arrest in multiple myeloma. *Blood*. 2010; 115(25):5202-13.
138. Zhang HT, Gui T, Sang Y, Yang J, Li YH, Liang GH, et al. The bet bromodomain inhibitor jq1 suppresses chondrosarcoma cell growth via regulation of yap/p21/c-myc signaling. *J Cell Biochem*. 2017; 118(8):2182-92.
139. Kelly KR, Nawrocki ST, Espitia CM, Zhang M, Yang JJ, Padmanabhan S, et al. Targeting aurora a kinase activity with the investigational agent alisertib increases the efficacy of cytarabine through a foxo-dependent mechanism. *Int J Cancer*. 2012; 131(11):2693-703.
140. Sharma V, Collins LB, Chen TH, Herr N, Takeda S, Sun W, et al. Oxidative stress at low levels can induce clustered DNA lesions leading to nhej mediated mutations. *Oncotarget*. 2016; 7(18):25377-90.
141. Zhao T, Sun Q, del Rincon SV, Lovato A, Marques M, Witcher M, et al. Gallotannin imposes s phase arrest in breast cancer cells and suppresses the growth of triple-negative tumors in vivo. *PLoS One*. 2014.
142. Jeggo Penny A, Löbrich M. How cancer cells hijack DNA double-strand break repair pathways to gain genomic instability. *Biochem J*. 2015; 471(1):1-11.

143. Ge X, Zhang Y, Huang F, Wu Y, Pang J, Li X, et al. Egfr tyrosine kinase inhibitor almonertinib induces apoptosis and autophagy mediated by reactive oxygen species in non-small cell lung cancer cells. *Hum Exp Toxicol*. 2021; 40(12\_suppl):S49-S62.
144. Sancho P, Bertran E, Caja L, Carmona-Cuenca I, Murillo MM, Fabregat I. The inhibition of the epidermal growth factor (egf) pathway enhances tgf- $\beta$ -induced apoptosis in rat hepatoma cells through inducing oxidative stress coincident with a change in the expression pattern of the nadph oxidases (nox) isoforms. *Biochimica et Biophysica Acta (BBA) - Molecular Cell Research*. 2009; 1793(2):253-63.
145. Dawei H, Honggang D, Qian W. Aurka contributes to the progression of oral squamous cell carcinoma (oscc) through modulating epithelial-to-mesenchymal transition (emt) and apoptosis via the regulation of ros. *Biochem Biophys Res Commun*. 2018; 507(1-4):83-90.
146. Truong TH, Carroll KS. Redox regulation of epidermal growth factor receptor signaling through cysteine oxidation. *Biochemistry*. 2012; 51(50):9954-65.
147. Shaalan AK, Teshima THN, Tucker AS, Proctor GB. Inhibition of aurora kinase b activity disrupts development and differentiation of salivary glands. *Cell Death Discovery*. 2021; 7(1).
148. Hussong M, Börno ST, Kerick M, Wunderlich A, Franz A, Sülmann H, et al. The bromodomain protein brd4 regulates the keap1/nrf2-dependent oxidative stress response. *Cell Death Dis*. 2014; 5(4):e1195-e.
149. Shi L, Xiong Y, Hu X, Wang Z, Xie C. Brd4 inhibition promotes trail-induced apoptosis by suppressing the transcriptional activity of nf-kb in nscl. *Int J Med Sci*. 2021; 18(14):3090-6.
150. Wu X, Liu D, Gao X, Xie F, Tao D, Xiao X, et al. Inhibition of brd4 suppresses cell proliferation and induces apoptosis in renal cell carcinoma. *Cell Physiol Biochem*. 2017; 41(5):1947-56.
151. Michael JM, You-Sun K, Zheng-gang L. Tnf $\alpha$  and reactive oxygen species in necrotic cell death. *Cell Res* 2008. p. 343-9.

## Thesis

### ORIGINALITY REPORT

<b>4%</b>	<b>3%</b>	<b>4%</b>	<b>%</b>
SIMILARITY INDEX	INTERNET SOURCES	PUBLICATIONS	STUDENT PAPERS

### PRIMARY SOURCES

<b>1</b>	<b>repository.up.ac.za</b> Internet Source	<b>2%</b>
<b>2</b>	<b>www.ncbi.nlm.nih.gov</b> Internet Source	<b>1%</b>
<b>3</b>	<b>Peifer, Christian, Rebecca Horbert, Boris Pinchuk et al. "Optimization of potent DFG-inhibitors of Platelet Derived Growth Factor Receptor<math>\beta</math> (PDGF-R<math>\beta</math>) guided by water thermodynamics", Journal of Medicinal Chemistry</b> Publication	<b>1%</b>

Exclude quotes  On      Exclude matches  < 1%  
Exclude bibliography  On



UNIVERSITEIT VAN PRETORIA  
 UNIVERSITY OF PRETORIA  
 YUNIBESITHI YA PRETORIA

Faculty of Health Sciences

**SUBMISSION FORM / RESUBMISSION FORM: MINI-DISSERTATION, DISSERTATION, THESIS**  
 (This form must be submitted together with the copies of the mini-dissertation, dissertation or thesis to the Student Administration office of the faculty)

STUDENT NUMBER: 11203367  
 Mr DF Joubert  
 PO Box 420  
 Mokolane  
 0600

(Please print)

Tel:	Mobile tel: 065 965 2131
Work address: 147 10th Avenue, Gezina, Pretoria	
Postal code: 0186	Tel:

Details of mini-dissertation/dissertation/thesis:

Programme: MSc	Plan: Human Physiology
Department:	PHYSIOLOGY
Supervisor:	PROF A PHULOKDAREE
Co-supervisor(s):	DR E NORTJE

Title of the mini-dissertation/dissertation/thesis:

(Exactly as approved by the postgraduate committee including upper case, lower case and punctuation)  
 High throughput in silico screening and in vitro testing of polypharmacological bromodomain 4 and cancer associated kinase inhibitor high throughput in silico screening and in vitro testing of polypharmacological bromodomain 4 and cancer associated kinase inhibitors

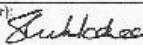
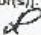
Statement by candidate:

1. I am aware that, should the mini-dissertation, dissertation or thesis be accepted, I must submit the additional copies as well as a copy of the draft article (Doctoral students: proof that it has been accepted for publication or published by an accredited journal) before 15 February for the Autumn graduation or before 15 July for the Spring Graduation as required by the relevant regulations and that the degree will not be conferred if this requirement has not been fulfilled.
2. I declare that the mini-dissertation, dissertation or thesis, which I hereby submit for the degree programme at the University of Pretoria, is my own work and has not previously been submitted by me for a degree at another university. Where secondary material is used, it has been carefully acknowledged and referenced in accordance with University requirements. I am aware of the University's policy and implications regarding plagiarism.

Signature: 	Date: 15 December 2022
--	------------------------

Statement by the Supervisor:

I hereby declare that I approve that Mr DF Joubert may submit his/her mini-dissertation/dissertation/thesis for examination. The co-supervisor has agreed to the submission.

Signature (Supervisor): 	Date: 15 DECEMBER 2022
Signature (Co-supervisor(s)): <i>in absentia</i> 	Date: 15 DECEMBER 2022

FOR OFFICE USE	
Received by:	Date:



Faculty of Health Sciences

**Institution:** The Research Ethics Committee, Faculty Health Sciences, University of Pretoria, complies with ICH-GCP guidelines and has US Federal wide Assurance.

- FWA 00002567 Approved dd 18 March 2022 and Expires 18 March 2027.
- ICRG #: ICRG0001762 OMB No. 0690-0278 Approved for use through August 31, 2023

Faculty of Health Sciences **Research Ethics Committee**

15 June 2022

**Approval Certificate  
Annual Renewal**

Dear Mr DF Joubert,

**Ethics Reference No.:** 252/2019 – Line 4

**Title:** High throughput in silico screening and in vitro testing of polypharmacological bromodomain 4 and cancer associated kinase inhibitors

The **Annual Renewal** as supported by documents received between 2022-05-18 and 2022-06-15 for your research, was approved by the Faculty of Health Sciences Research Ethics Committee on 2022-06-15 as resolved by its quorate meeting.

Please note the following about your ethics approval:

- Renewal of ethics approval is valid for 1 year, subsequent annual renewal will become due on 2023-06-15.
- Please remember to use your protocol number (252/2019) on any documents or correspondence with the Research Ethics Committee regarding your research.
- Please note that the Research Ethics Committee may ask further questions, seek additional information, require further modification, monitor the conduct of your research, or suspend or withdraw ethics approval.

Ethics approval is subject to the following:

- The ethics approval is conditional on the research being conducted as stipulated by the details of all documents submitted to the Committee. In the event that a further need arises to change who the investigators are, the methods or any other aspect, such changes must be submitted as an Amendment for approval by the Committee.

We wish you the best with your research.

Yours sincerely

On behalf of the FHS REC, Dr R Sommers  
MBChB, MMed (Int), MPharmMed, PhD  
Deputy Chairperson of the Faculty of Health Sciences Research Ethics Committee, University of Pretoria

The Faculty of Health Sciences Research Ethics Committee complies with the SA National Act 61 of 2003 as it pertains to health research and the United States Code of Federal Regulations Title 46 and 45. This committee abides by the ethical norms and principles for research, established by the Declaration of Helsinki, the South African Medical Research Council Guidelines as well as the Guidelines for Ethical Research: Principles Structures and Processes, Second Edition 2016 (Department of Health)

Research Ethics Committee  
Room 1 00, Level 1, 12voelkies Building  
University of Pretoria, Private Bag 823  
Gauteng 0001, South Africa  
Tel: (+27) 011 4296 4051  
Email: [ethics@hscs.up.ac.za](mailto:ethics@hscs.up.ac.za)  
[www.up.ac.za](http://www.up.ac.za)

Isikwetho: Ukwazi nokwazi/Information  
Litsigano la Ubuciko/EO Wapholile